Contrib Mineral Petrol (2013) 166:1593–1611
DOI 10.1007/s00410-013-0944-8

ORIGINAL PAPER

Experimental phase relations of a low MgO Aleutian basaltic andesite at $XH_2O = 0.7–1$

Erika L. Rader · Jessica F. Larsen

Received: 11 December 2012 / Accepted: 21 September 2013 / Published online: 9 October 2013

Abstract We conducted melting experiments on a low MgO (3.29 wt.%) basaltic andesite (54.63 wt.% SiO_2) from Westdahl volcano, Alaska, at $XH_2O = 0.7–1$ and $fO_2 \sim$ Ni–NiO, at pressures = 0.1–180 MPa and temperatures = 900–1,200 °C. We examine the evolution of the melt along a liquid line of descent during equilibrium crystallization at high H_2O and fO_2 conditions, starting from a high FeOt/MgO, low MgO basaltic andesite. Ti-magnetite formed on the liquidus regardless of XH_2O, followed by clinopyroxene, plagioclase, amphibole, and orthopyroxene. We observe slight but significant differences in the phase stability curves between the $XH_2O = 1$ and 0.7 experiments. Early crystallization of Ti-magnetite and suppression of plagioclase at higher pressures and temperatures resulted in strongly decreasing melt FeOt/MgO with increasing SiO_2, consistent with a "calc-alkaline" compositional trend, in agreement with prior phase equilibria studies on basalt at similar H_2O and fO_2. Our study helps quantify the impact of small amounts of CO_2 and high fO_2 on the evolution of melts formed during crystallization of a low MgO basaltic andesite magma stored at mid- to shallow crustal conditions. Like the prior studies, we conclude that H_2O strongly influences melt evolution trends, through stabilization of Ti-magnetite on the liquidus and suppression of plagioclase at high P–T conditions.

Communicated by G. Moore.

E. L. Rader
Department of Geological Sciences, University of Idaho, Moscow, ID 83844, USA

J. F. Larsen (✉)
Geophysical Institute and Department of Geology and Geophysics, University of Alaska, Fairbanks, AK 99775, USA
e-mail: jflarsen@alaska.edu

Keywords Basaltic andesite · Westdahl volcano · Aleutians · Phase equilibria · Melting experiments

Introduction

Primitive arc magmas are generated in the mantle wedge or at the slab interface by several possible partial-melting scenarios (e.g., Kelley et al. 2006; Tatsumi et al. 1983; Yogodzinski and Kelemen 1998). They are then modified during ascent by assimilation and fractional crystallization (AFC) and magma mixing processes (e.g., Annen et al. 2006). Despite overarching questions about the role of differentiation and the liquid line of descent versus the importance of repeated replenishment, hybridization, and "crustal" contamination in creating arc magma series (Annen et al. 2006; Eichelberger et al. 2006), it is instructive to assess primary controls on melt evolution through controlled high-pressure and temperature experiments. Experiments provide a way to examine how different isolated parameters, such as bulk and fluid compositions and/or fO_2, influence melt compositional evolution during equilibrium crystallization.

Arc magmas are often classified according to two predominant compositional series, typically defined by calc-alkaline (CA) or tholeiitic (TH) differentiation trends (e.g., Kay et al. 1982; Zimmer et al. 2010). The term "calc-alkaline" strictly refers to the alkali-lime index and where the intersection between $K_2O + Na_2O$ and CaO compositions occurs in terms of SiO_2 (e.g., Peacock 1931; Arculus 2003). However, other criteria that depend on the FeOt/MgO ratio of the magmas (Kuno 1968; Irvine and Baragar 1971; Miyashiro 1974) are commonly applied to both natural and experimental samples to discriminate between different magma series.

Many prior experimental studies (e.g., Baker and Eggler 1983; Eggler and Burnham 1973; Grove and Baker 1984;

Sisson and Grove 1993a, b; Kawamoto 1996; Moore and Carmichael 1998; Blatter and Carmichael 2001; Hammer et al. 2002; Berndt et al. 2005; Di Carlo et al. 2006) have examined various conditions that influence the differentiation trends observed in experimental melts during equilibrium crystallization. Two primary controls have emerged as major influences on the FeOt of the experimental melts: H_2O content and oxygen fugacity (fO_2). Studies focused on basalt and basaltic andesite starting compositions indicate that relatively high melt H_2O suppresses plagioclase crystallization and favors Fe- and, to a lesser degree, Mg-bearing mafic minerals early in the crystallization sequence (e.g., Moore and Carmichael, 1998; Sisson et al. 2005; Tatsumi and Suzuki 2009). This causes the melt to evolve to lower FeOt relative to MgO as SiO_2 increases. Other studies reveal that fO_2 influences the crystallization sequence of mafic silicate phases and Fe–Ti oxides, with melt Mg# changing with fO_2 (Feig et al. 2010). In general, it appears that H_2O exerts the major control on melt differentiation pathways with regard to FeOt enrichment or depletion. Oxygen fugacity is also important, but H_2O can influence the trends to a greater degree even with significant reduction in fO_2 (e.g., Feig et al. 2010).

The focus of this study is to examine the experimental phase relations in a low MgO Aleutian basaltic andesite at $XH_2O = 0.7$ to 1, at relatively high fO_2 = Ni–NiO (NNO) at mid- to shallow crustal conditions. Our data provide an evolutionary link between basalt and more evolved crustal magmas by examining phase equilibria in a low MgO basaltic andesite at relatively high fO_2 and H_2O contents found in some subduction zone volcanoes. The starting material likely represents magma that has already experienced fractionation of olivine, has high FeOt/MgO, and is strongly "tholeiitic" (Miyashiro 1974). We use this composition to examine the effect of high H_2O and fO_2 on melt compositional evolution during further crystallization at mid- to shallow crustal conditions. Regardless of starting XH_2O, Ti-magnetite forms on the liquidus, causing the melt to rapidly decrease in FeOt/MgO, consistent with a "calc-alkaline" differentiation trend (e.g., Miyashiro 1974), despite the strongly "tholeiitic" bulk starting composition. Our results generally agree with other studies with basaltic starting compositions (e.g., Tatsumi and Suzuki 2009) at similar fO_2 and H_2O contents, showing that changes in crustal magmatic conditions could greatly influence shallow evolution of arc magmas.

Methods

Experimental methods

Melting experiments were conducted using natural tholeiitic basaltic andesite from Westdahl volcano, in the eastern Aleutian Islands, Alaska. All experiments employed a finely crushed natural bomb sample (MW98-16; Table 1) obtained from Richard Moore (US Geological Survey), collected from a scoria deposit produced by lava fountaining during the 1991–1992 eruption. Because the powdered starting materials contain relict broken phenocrysts and microlites, we conducted melting experiments at high temperatures and pressures where local equilibrium between experimental melt and growing crystals is more quickly attained. Two series of experiments were run: $XH_2O = 1$ and $XH_2O = 0.71$ to 0.75 ($\sim$0.7; Table 2). More than 60 experiments were run, filtered to 38 after discarding experiments that did not achieve local equilibrium, as described in the discussion section. Experiments were run at total pressures (P_{Total}) between 0.1 and 180 MPa and temperatures between 900 and 1,200 °C (Table 2).

Experiments at 0.1 MPa were run in a vertical tube furnace using mixed H_2:CO_2 gases to fix oxygen fugacity at approximately Ni–NiO. The furnace temperature was measured in situ about 1 cm from the sample using Pt-$Pt_{90}Rh_{10}$ thermocouple calibrated against the melting point of gold. Oxygen fugacity was measured using Yt-stabilized zirconia sensor and platinum electrodes, using air as the reference gas (Sato 1971). The powdered starting material was bound with polyvinyl alcohol and suspended on fine platinum wire that had been treated with Fe after Grove (1981) and Grove and Juster (1989). The experiments were run at 1,133–1,181 °C for 70–93 h and were rapidly quenched by running an electrical current through the wire hanger, dropping the experiment into a cup of water.

High-pressure experiments above 1,050 °C were conducted using $Au_{75}Pd_{25}$ capsules. Sample powders were contained in an unsealed, 3 mm outer diameter (OD) capsule enclosed within a larger, sealed 5 mm OD capsule, along with the desired fluid mixture (described below) and a platinum capsule containing Ni foil and NiO powder compounds to control fO_2. The inner capsules were pre-treated to mitigate iron loss by running the MW98-16 starting powders in the 1 atmosphere gas mixing furnace at $fO_2 \sim$ Ni–NiO at 1,200 °C for 48 to 72 h (Kawamoto and Hirose 1994), which should be sufficient to form an alloy within the innermost portion of the sample capsule, adjacent to the experimental melt. Because our experiments were conducted at high fO_2 and XH_2O in the fluid, we expect Fe loss to be relatively small (Kawamoto and Hirose 1994).

High-pressure experiments conducted below 1,050 °C were run in Au capsules. The starting powders were loaded directly into a 4-mm-OD Au capsule, along with the fluid mixtures and the platinum buffer capsule, omitting the separate, Fe pre-treated inner sample capsule. Both the 5-mm $Au_{75}Pd_{25}$ and 4-mm Au outer capsules were welded

Table 1 Starting composition

Sample	SiO_2	TiO_2	Al_2O_3	FeO_t	MnO	MgO	CaO	Na_2O	K_2O	P_2O_5	Total[a]
MW98-16	54.63	1.73	15.82	10.82	0.24	3.29	7.38	4.5	1.25	0.35	99.18

[a] Analyses normalized to 100 %, with original total reported

closed using an oxygen–acetylene torch. All experiments were run for 6–126 h, with run times dictated by the P–T conditions, as compared with prior studies using similar composition starting powders (Blatter and Carmichael 2001; Moore and Carmichael 1998). Experiments run below 1,100 °C were conducted in Titanium–Zirconium–Molybdenum (TZM) alloy pressure vessels surrounded by an outer inconel sheath and bathed in argon gas. Experiments conducted at temperatures above 1,100 °C required use of Molybdenum–Hafnium–Carbide (MHC) vessels, which extended the temperature range up to 1,200 °C for the super-liquidus experiments conducted at pressures up to 150 MPa (Table 2). Temperature was controlled externally by a DelTech DT-31 furnace and was calibrated using a K-type thermocouple, by mapping the temperature within the vessel at appropriate furnace set points before batches of experiments were run. Thermal gradients within the bottom of the vessel varied to within ±5 °C over ~2.5 cm length, which is equivalent to the lengths of the experimental capsules. Pressure was monitored using a Heise pressure gauge with an accuracy of ±1 MPa as determined by the manufacturer. Hydrogen loss from the experimental capsules was mitigated by adding ~0.25 MPa of CH_4 to the argon gas pressurizing the vessel. This served to help maintain fO_2 at approximately Ni–NiO by buffering fH_2 inside the pressure vessel.

Each experiment was rapidly quenched after Sisson and Grove (1993a), which helped mitigate quench crystallization. The samples were extracted from the metal capsules after the total weight of the charge was recorded. If the post-experiment weight differed from the original by >0.0005 g, the experiment was discarded. If the total weight did not decrease and a fluid phase was present upon puncturing the capsule, the buffer capsule was recovered and opened to determine whether both Ni and NiO were present. Experiments that did not contain both buffering compounds at the end of the run were also discarded because of poorly constrained fO_2.

$XH_2O = 1$ experiments were loaded with ~10 wt % de-ionized H_2O to ensure vapor saturation, along with 0.15–0.2 g of sample powder. Experiments conducted at $XH_2O < 1$ configured for $XH_2O \sim 0.7$ and $XCO_2 \sim 0.3$ in the fluid on a molar basis by weighing Ag_2CO_3 or oxalic acid powders (WD05 and WD06) to H_2O proportionately to water to achieve the desired XCO_2 (e.g., Botcharnikov et al. 2005; Eggler 1972; Eggler and Burnham 1973; Hammer et al. 2002; Holloway et al. 1968). The volume of oxalic acid needed to create the desired XCO_2 was rather large so we relied on Ag_2CO_3 powder for the majority of the runs. The resulting XCO_2 varies between ~0.25 and 0.31, with an average of 0.73 (±0.02; Table 2). Hereafter, we abbreviate XH_2O as 0.7 in mixed fluid experiments.

Analytical methods

Electron microprobe analyses

Experimental sample chips were embedded in Hilquist epoxy and glued to a petrographic slide using acetone soluble Crystalbond 509. Each sample was polished to a 1-μ finish on a single side suitable for electron microprobe and then the glassiest experiments were doubly polished for transmission FTIR analyses. Crystal phases were identified first using a petrographic microscope, and then, the samples were carbon coated for subsequent analysis by electron microprobe. Quantitative analyses of the experimental phases were obtained at the University of Alaska Advanced Instrumentation Laboratory on a Cameca SX-50 microprobe equipped with four wavelength dispersive spectrometers and an EDAX energy dispersive spectrometer. A 15 keV, 10nA, focused beam (~2 μm) was used for mineral analyses. Count times and beam conditions allowed for detection limits on individual elements of 0.08 wt % or better. Working standards 228 plagioclase (labradorite), diopside (306, 208), rhyolite glass (KN-18), and basaltic glasses (BG1, 2, and 3) were run to assess the calibrations.

Hydrous glass analyses were conducted using a 15 keV, 10 nA defocused beam (10 μm) to mitigate Na migration (Morgan and London 1996). Sodium was analyzed first and a time-dependent Na count decay curve was generated using the self-calibrated, Na migration routine within Probe for Windows© software package. From this curve, initial Na counts were corrected back to their original estimated values.

Micro-FTIR H_2O and CO_2 analyses

H_2O and CO_2 concentrations were measured in glasses from a subset of the samples using a Thermo Scientific Nicolet 6700 Fourier Transform Infrared (FTIR) spectrometer with Continμum microscope equipped with

Table 2 Experimental run conditions and products

Run	Time (h)	XCO_2	T (°C)	P_{Tot} (MPa)	Phases[a]
WDL_8[d]	66	–	1,262	0.1	g(1)
WDL_12	70	–	1,181	0.1	gl(0.73), pl(0.26)[b]
WDL_11	89	–	1,161	0.1	gl, pl
WDL_10	93	–	1,133	0.1	gl, pl, ox, ol
WD03	48	0.25	1,000	100	gl, pl, cpx, ox
WD05	47	0.25	975	94	gl(0.6), pl(0.1), cpx(0.2), ox (0.1)
WD06	47	0.26	1,025	75	gl (0.7), pl(0.15), cpx(0.08), ox(0.07)[b]
WD07	6	0.26	1,200	100	gl (1)
WD08	6	0.26	1,150	150	gl (1)
WD09	6	0.26	1,170	50	gl (1)
WD10	24	0.26	1,050	75	gl, ox
WD12	48	0.26	1,000	150	gl, pl, cpx, ox, amph
WD13	24	0.26	1,075	75	gl, ox
WD15	24	0.27	1,100	25	gl, ox
WD16	33	0.27	1,050	100	gl, ox
WD18	48	0.27	1,025	100	gl(0.74), pl(0.1), cpx(0.1), ox(0.06)[b]
WD20	48	0.28	975	100	gl(0.88), pl(0.06), cpx(0.02), opx(0.01), ox(0.03)[c]
WD21	23	0.28	1,050	75	gl, ox
WD22	48	0.29	1,025	150	gl, ox, px
WD23	48	0.29	900	100	gl, pl, cpx, ox
WD24	48	0.29	1,000	180	gl, cpx, ox, amph
WD27	47	0.31	900	100	gl(0.67), pl(0.09), cpx(0.16), ox(0.08)[c]
WD30	48	–	950	125	gl(0.74), cpx(0.11), pl(0.12), ox(0.04), amph(n/a)[c]
WD31	49	–	975	120	gl(0.07), cpx(0.13), pl(0.04), ox(0.07), amph(n/a)[b]
WD33	126	–	1,000	75	gl, cpx, pl, ox
WD35	48	–	975	92	gl(0.7), cpx(0.09), pl(0.18), ox(0.03)[c]
WD37	6	–	1,150	100	gl(1)
WD38	6	–	1,150	150	gl(1)
WD39	6	–	1,165	50	gl(1)
WD40	48	–	1,050	50	gl, ox
WD41	24	–	1,100	50	gl, ox
WD42	25	–	1,050	75	gl, ox
WD44	24	–	1,075	75	gl(1)
WD47	49	–	1,000	120	gl(0.85), cpx(0.07), ox(0.08)[b]
WD51	48	–	950	100	gl(0.4), pl(0.31), cpx(0.20), ox(0.07), amph(n/a)[b]
WD52	113	–	925	100	gl(0.22), cpx(0.20), opx(<0.01), pl(0.49), ox(0.08)[b]
WD55	43	–	1,020	100	gl, cpx, ox
WD56	24	–	1,000	182	gl, cpx, ox, amph
WD58	54	–	1,040	150	gl, cpx, ox
WD60	48	–	1,025	160	gl, ox
WD61	48	–	950	50	gl, cpx, pl, ox
WD62	48	–	975	150	gl(0.7), pl(0.08), cpx(0.15), ox(0.09), amph(n/a)[b]

[a] gl-glass; pl-plagioclase; cpx-clinopyroxene; ox-oxides (Ti-magnetite); amph-amphibole; opx-orthopyroxene

[b] Phase proportions included in parentheses, calculated by mass balance, with root mean square error on the least squares solution for all phases (lscov function in MatLab) as follows: WD06 = 0.05; WD11 = 0.03; WD14 = 0.30; WD18 = 0.07; WD31 = 0.04; WD47 = 0.21; WD51 = 0.03; WD52 = 0.02; WD62 = 0.10

[c] Phase proportions estimated by image analysis

[d] The 0.1 MPa experiments had measured log fO_2 as follows: WDL_8 = −7.45 (0.08); WDL_12 = −7.82 (0.04); WDL_11 = −8.10 (0.07); WDL_10 = −8.41 (0.22)

standard and 50-micron (high spatial resolution) MCT-A detectors. Only experiments with clean, microlite-free glass regions at least 50 × 50 microns across were selected for analysis. Doubly polished sample chips were placed on a NaCl disk and analyzed using transmission FTIR methods, with each spectra consisting of 512 scans and 4 cm^{-1} resolution. Infrared absorbance for H_2O + OH species was measured for the 5,200 cm^{-1} H_2O, 4,500 cm^{-1} OH, and 3,550 cm^{-1} H_2O + OH absorption bands. Spectra of the experiments run at $XH_2O < 1$ were examined for dissolved CO_2 and CO_3^{2-} species (Blank and Brooker 1994; King et al. 2002) but difficulties in resolving the 1,420 and 1,560 cm^{-1} CO_3^{2-} peaks were encountered. Similar to Behrens et al. (2004), H_2O-rich samples of high Al content basaltic andesite and andesite glasses from our experimental runs created large molecular H_2O (1,630 cm^{-1}) and silicate absorption bands that effectively obscured peaks in the CO_3^{2-} spectral region. Although up to ~300 ppm CO_2 is expected in our experiments, the likely obscuration of those peaks due to the high background and neighboring H_2O and silicate bands made it impossible to resolve measurable CO_2. Lack of an appreciable CO_2 peak at 2,350 cm^{-1} indicates that the majority of the CO_2 is dissolved as CO_3^{2}, in agreement with other studies (King et al. 2002).

Total dissolved water contents were calculated using the Beer–Lambert equation:

$$A_n = C * \rho * t * \varepsilon_n / 18.02 \quad (1)$$

where A_n is the absorbance at each peak n, C is the concentration of each water species in weight percent for an absorption band, t is sample thickness, ε_n is the wavelength and compositionally dependent molar absorptivity of the glass. Glass densities (ρ) were calculated after Lange and Carmichael (1987) based on their compositions determined by electron microprobe for each sample. We used ε appropriate for andesites because the glasses analyzed are generally between 57 and 63 wt.% SiO_2: 1.07 L/mol/ cm^{-1} for 5,200 cm^{-1}, 0.79 L/mol/ cm^{-1} for 4,500 cm^{-1} derived from Fe-bearing andesites (Mandeville et al. 2002) and 70.3 L/mol/ cm^{-1} for 3,550 cm^{-1} for a Mount Hood andesite (King et al. 2002). Sample thicknesses, ranging between 20 to 100 μm, were measured on each spot analyzed using reflectance spectroscopy after Nichols and Wysoczanski (2007):

$$t = m/(2\eta(v2 - v1)) \quad (2)$$

where m is the number of interference fringes within a selected wavenumber interval v2–v1, and n is the compositionally dependent refractive index of the glass, calculated using Church and Johnson (1980). Reflectance spectra involved collecting 240 scans on each spot analyzed using transmission spectra and referencing each reflectance spectra to the background obtained from a polished, gold-coated mirror.

Results

Experimental fO_2

We maintained fO_2 in our experiments approximately along the Ni–NiO (NNO) buffer using separate buffer capsules containing Ni metal foil and NiO powder and buffered against H_2 loss through the capsule walls by adding CH_4 to the argon pressurizing gas (e.g., Hammer et al. 2002). However, a decrease in fO_2 is expected in experiments with $XH_2O < 1$, because of decreasing fH_2O (e.g., Freise et al. 2009; Scaillet et al. 1995). Because we did not measure fH_2 or fO_2 directly using Ni–Pd sensor capsules or Shaw membrane (Pownceby and O'Neill 1994; Scaillet et al. 1992; Shaw 1963; Taylor et al. 1992), it is not possible to calculate fO_2 in our experiments precisely based on the H_2O dissociation reaction (e.g., Freise et al. 2009; Scaillet et al. 1995). Therefore, it is possible that fO_2 was reduced in the $XH_2O = 0.7$ experiments, but we could not observe the amount of reduction. However, the presence of both Ni metal and NiO powder in the buffer capsules at the end of each successful experiment indicates that fO_2 was maintained approximately along the Ni–NiO buffer, even in experiments with reduced XH_2O. In similar experiments conducted on andesite from Novarupta, Hammer et al. (2002) employed the same method in the TZM cold-seal apparatus and interpreted the absence of Ni metal foil in the buffer capsules at the end of the run to signify a modest shift in fO_2 to no more than NNO + 2 log units. Because we discarded runs that did not also contain Ni after quenching, we estimate that our acceptable experiments probably were within 1 log unit of NNO.

Experimental results

Mineral phases crystallized in all experiments (Figs. 1, 2, 3), except for the highest temperature runs that contain only glass (Table 2). At progressively lower temperatures, the minerals appear in the order of Ti-magnetite, clinopyroxene, plagioclase, amphibole, and orthopyroxene between the pressures of 25–180 MPa and temperatures of 900–1,100 °C (Table 2). At 0.1 MPa, plagioclase is on the liquidus, followed by magnetite and olivine. We did not find stable olivine in any of the high-pressure experiments.

Mineral phase proportions increase with decreasing melt fraction and increasing glass SiO_2 content as expected (Fig. 4). In experiments run at both $XH_2O = 1$ and 0.7, Ti-magnetite is the liquidus phase (Figs. 2, 3). Orthopyroxene is the lowest temperature mineral, forming below

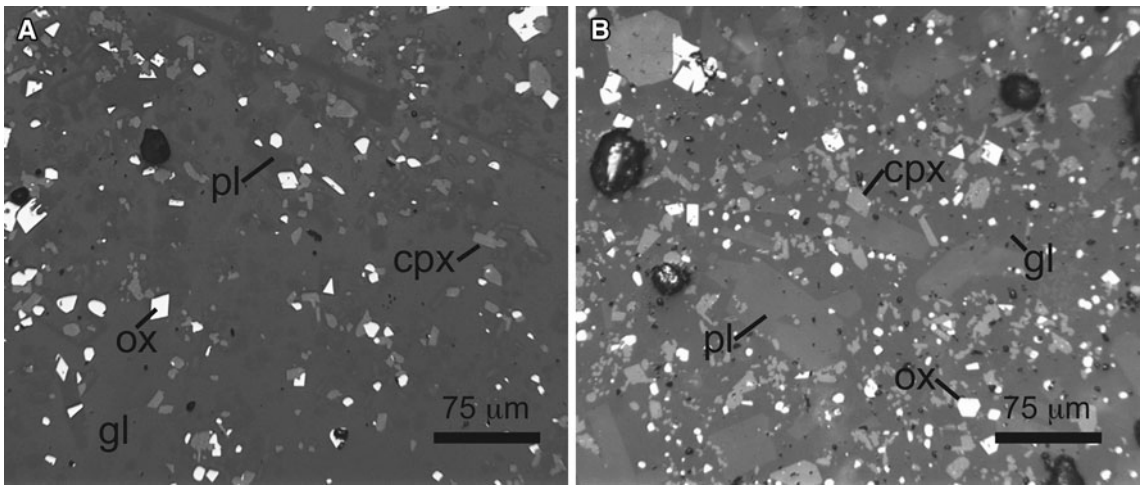

Fig. 1 Representative reflected light photomicrographs of two experiments. Examples of the three most prominent mineral phases (*ox* oxides; *pl* plagioclase; and *cpx* clinopyroxene) are noted. **a** Experiment WD24 at $XH_2O = 0.71$, $P_{Total} = 180$ MPa, T = 1,000 °C. Regions of glass are also noted (gl). **b** Experiment WD34 at $XH_2O = 1$, $P_{Total} = 135$ MPa, T = 950 °C

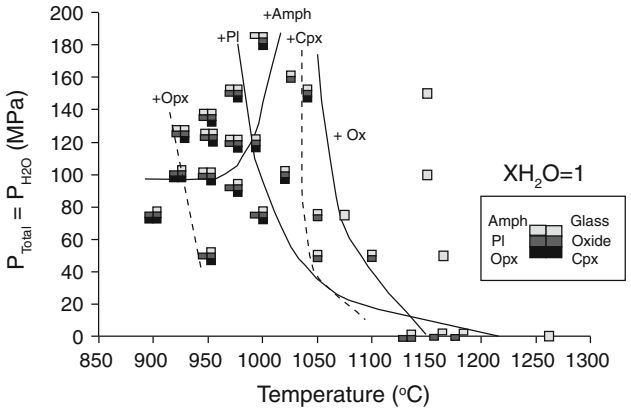

Fig. 2 Phase diagram of low MgO Aleutian basaltic andesite (Westdahl 1992; MW98-16) at $XH_2O = 1$ ($P_{H2O} = P_{Total}$), redox conditions controlled along Ni–NiO buffer. Phase-in curves are labeled as follows: Ti-magnetite (oxide), clinopyroxene (cpx), plagioclase (pl), amphibole (amph), orthopyroxene (opx). The *curves* are shown as *solid lines* where the position is more certain, and *dashed lines* where the position is less well constrained. Minerals found in each experiment are denoted by the *shading* in the *symbols*, as shown in the legend

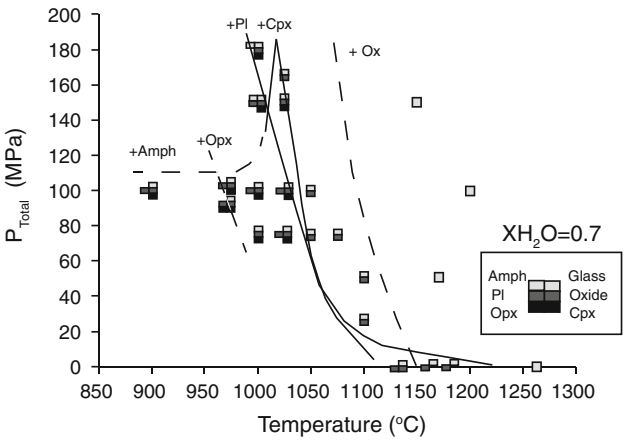

Fig. 3 Phase diagram of Westdahl (MW98-16) basaltic andesite at $XH_2O \sim 0.7$ and redox conditions controlled along Ni–NiO buffer. Phase-in curves are labeled as follows: Ti-magnetite (oxide), clinopyroxene (cpx), plagioclase (pl), amphibole (amph), orthopyroxene (opx). The *curves* are shown as *solid lines* where the position is more certain, and *dashed lines* where the position is less well constrained. Minerals found in each experiment are denoted by shaded symbols, as shown in the legend

~925 °C. Despite the presence of olivine in the natural samples, it was not observed in the experimental run products at pressures between 25 and 180 MPa. It is possible either that the P–T region of olivine stability is very narrow and was not captured by the pressures and temperatures employed, or olivine simply is not stable at the relatively oxidizing $fO_2 \sim$ Ni–NiO, in water-rich experiments of this MgO-poor basaltic andesite.

There is a very small difference in liquidus temperatures between the $XH_2O = 1$ and 0.7 experiments, whereby Ti-magnetite appears to form approximately 10 °C cooler in the $XH_2O = 1$ experiments at low dissolved melt H_2O concentrations (Fig. 5). Plagioclase crystallizes ~25 °C higher at $XH_2O = 0.7$ than $XH_2O = 1$, and the temperature difference becomes progressively smaller as melt H_2O content increases (Fig. 5). There is little difference in the clinopyroxene stability curves between the $XH_2O = 1$ and 0.7 experiments.

Experimental glass compositions

Super-liquidus experiments have glass compositions similar to the bulk starting material within about 1 wt.% (e.g., WD15 = 55.36 ± 0.56 compared to 54.63 wt.% SiO_2 in

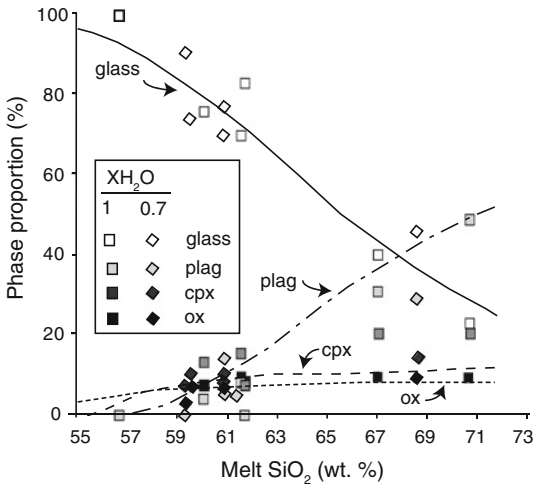

Fig. 4 Experimental phase proportions (symbols) plotted with those predicted by MELTS (solid and dashed curves; Ghiorso and Sack 1995; Asimow and Ghiorso 1998). The legend shows *squares* ($XH_2O = 1$) and *diamonds* ($XH_2O = 0.7$) *shaded* to represent each phase. The *curves* represent MELTS model predicted phase proportions: *solid curve* is the MELTS calculation for glass; *dash-dot curve* plagioclase; *long dashed curve* clinopyroxene; *short dashed curve* oxides

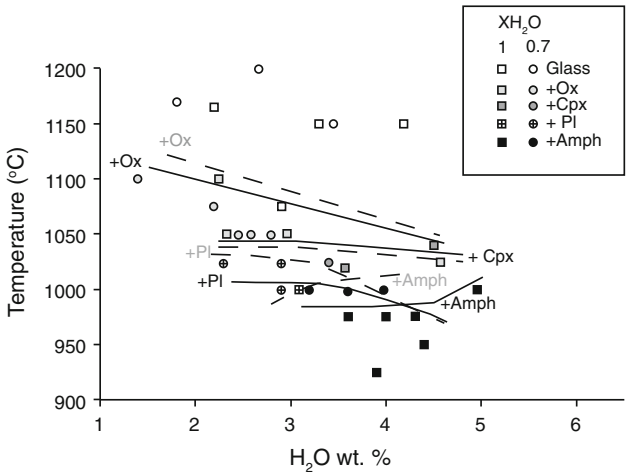

Fig. 5 Phase curves plotted as temperature versus H_2O concentration measured or modeled (Moore et al. 1998) in the experimental melt. The *symbols* for experiments containing each mineral phase are given in the legend. The *solid curves* are the approximate locations of the phase stability boundaries in the $XH_2O = 1$ series. The *dashed curves* are those estimated for the $XH_2O \sim 0.7$ series. Experiments with measured H_2O concentrations (FTIR) are reported in Table 3. Those with calculated H_2O contents based on the measured glass compositions (Moore et al. 1998) are as follows (in wt.% H_2O): WD03 = 2.9; WD06 = 2.3; WD07 = 2.7; WD08 = 3.5; WD09 = 1.8; WD10 = 2.5; WD12 = 3.2; WD18 = 2.9; WD24 = 4.0; WD31 = 4.0; WD33 = 3.1; WD37 = 3.3; WD38 = 4.2; WD39 = 2.2; WD40 = 2.3; WD41 = 2.3; WD42 = 3.0; WD44 = 2.9; WD51 = 4.4; WD52 = 3.9; WD55 = 3.6; WD56 = 5.0; WD58 = 4.5; WD59 = 4.5; WD60 = 4.6; WD62 = 4.3

MW-98). Regardless of experimental XH_2O, the melt phase evolved toward dacitic compositions along similar trends in the major oxides (Fig. 6). Individual oxides TiO_2, MgO, CaO, and FeOt decrease and K_2O and Na_2O increase along the same trends, likely reflecting the similarity in changing pyroxene and Ti-magnetite phase proportions in both experimental series (Fig. 4). A small difference is observed in Al_2O_3 as SiO_2 increases to 68 wt.% at $XH_2O = 0.7$, with a slight apparent depletion in Al_2O_3 by about 0.5–1 wt.% when compared with the $XH_2O = 1$ trend. It is possible that this is caused by the 25 °C higher plagioclase stability field in the $XH_2O = 0.7$ series (Figs. 2, 3, 5), causing a slight increase in plagioclase contents and a small depletion in glass Al_2O_3.

FTIR analyses collected from experiments with enough glass for clean measurements indicate dissolved water concentrations vary as a function of pressure, as expected (Fig. 7; Table 3). Select experiments from the $XH_2O = 1$ series vary between 2.3 and 3.9 wt.% total H_2O at pressures between 50 and 120 MPa (975 to 1,050 °C; Fig. 7) and those from the $XH_2O = 0.7$ experiments contain 1.4–3.4 wt.% total H_2O at pressures between 25 and 150 MPa (1,000–1,100 °C; Fig. 7). The experiments agree well with solubility curves calculated after Moore et al. (1998) based on the experimental glass compositions and estimated $XH_2O = 1$ or 0.7 for each series, verifying that they achieved the desired H_2O:CO_2 fluid phase composition. Thus, the similarities seen between the phase compositions are real and not an artifact of imprecise experimental fluid compositions.

Experimental plagioclase

Euhedral plagioclase crystallized in the experiments, varying in composition as a function of total pressure and temperature (Fig. 8). Overall, plagioclase varies from An_{38} to An_{63} at $XH_2O = 1$ and An_{25} to An_{59} at $XH_2O = 0.7$. The range in An contents is similar to those from other experimental studies on basaltic andesite to andesite bulk compositions at pressures of 200 MPa or less (e.g., $An_{49\text{-}65}$, Blatter and Carmichael 2001; $An_{57\text{-}76}$; Moore and Carmichael 1998), except for the lowest An content plagioclase ($An_{25\text{-}38}$) analyzed in the lowest P–T, highest crystallinity experiments from this study. Plagioclase An content increases systematically with increasing temperature (900–1,025 °C) at pressures that fall mainly between 75 and 120 MPa (Fig. 8a). Although scattered, there is also an approximate trend of increasing $K_D(Ca-Na)^{Plag}_{Liq}$ (molar $Ca/Na_{plag}/Ca/Na_{liq}$) as a function of the estimated activity of water (aH_2O), estimated after Burnham (1979), shown in Fig. 8b.

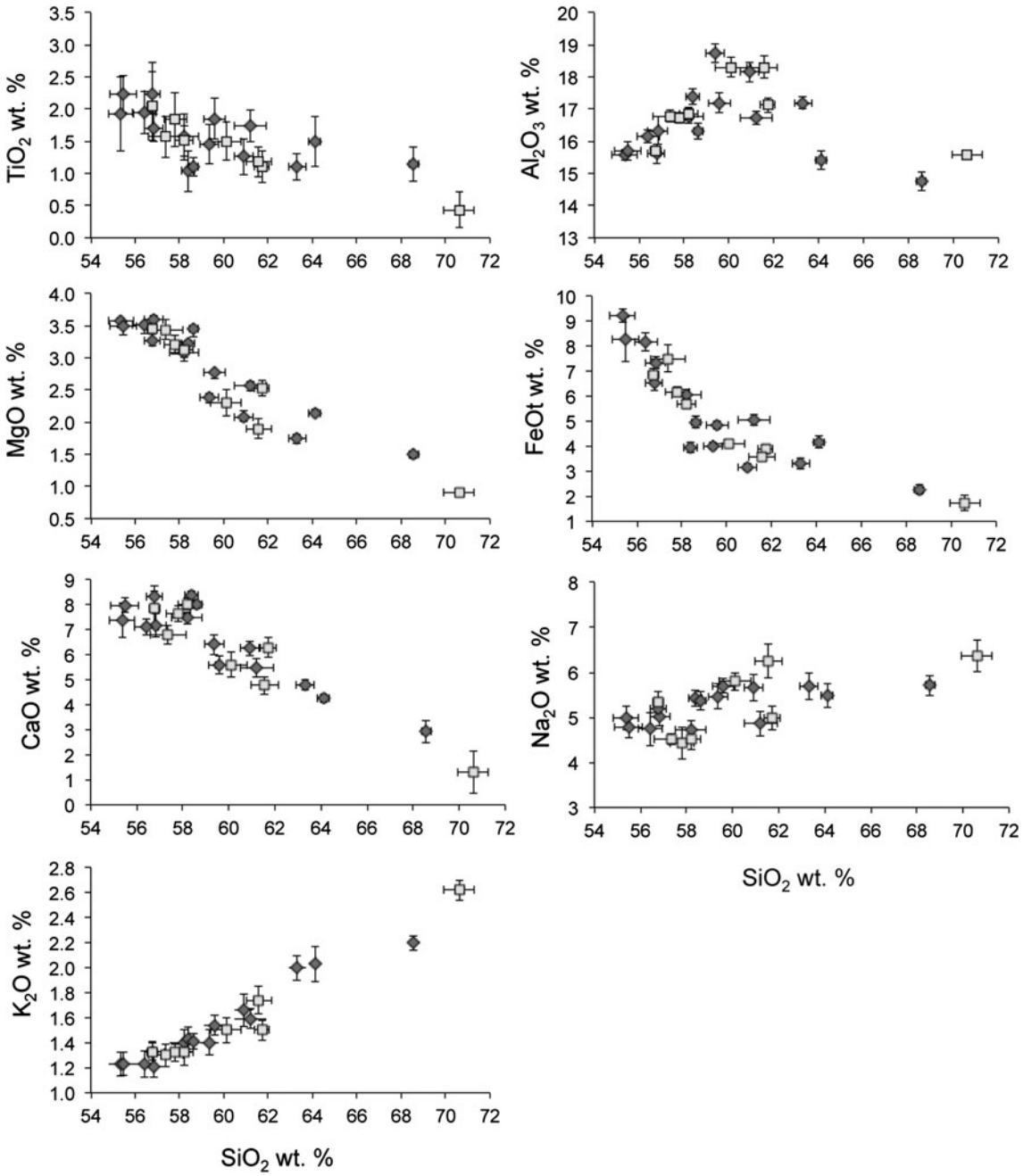

Fig. 6 Harker variation *diagrams* showing the experimental glass compositions for $XH_2O = 1$ (*dark gray diamonds*) and $XH_2O \sim 0.7$ experiments (*light gray squares*). Both series produce glass compositions that evolve to >68 wt.% SiO_2 along similar trends. A possibly small difference exists between the series in Al_2O_3 at SiO_2 greater than ~68 wt.%

To assess whether the plagioclase equilibrated with the co-existing melt, we used the model of Putirka (2008) to calculate $K_D(Ab-An)^{pl-liq}$ $(X^{pl}_{Ab}X^{liq}_{AlO_{1.5}}/X^{pl}_{An}X^{liq}_{NaO_{0.5}}X^{liq}_{SiO_2})$ with $K_D = 0.1 \pm 0.05$ for T < 1,050 °C and 0.27 ± 0.11 for T ≥ 1,050 °C. We performed the calculation for a subset of experiments from which both glass and plagioclase compositions are known. Experiments from the $XH_2O = 0.7$ series have $K_D(Ca-Na)^{pl-liq}$ between 0.1 and 0.13 (WD03 = 0.1, WD06 = 0.13, WD12 = 0.1, WD18 = 0.13). Those from the XH_2O series have $K_D(Ab-An)^{pl-liq}$ between 0.04 and 0.12 (WD31 = 0.12; WD51 = 0.09; WD52 = 0.04; WD62 = 0.08). The $K_D(Ab-An)^{pl-liq}$ of WD52 falls just slightly out of the equilibrium range cited by Putirka (2008). Thus, it is possible that those plagioclase compositions did not completely equilibrate after 113 h.

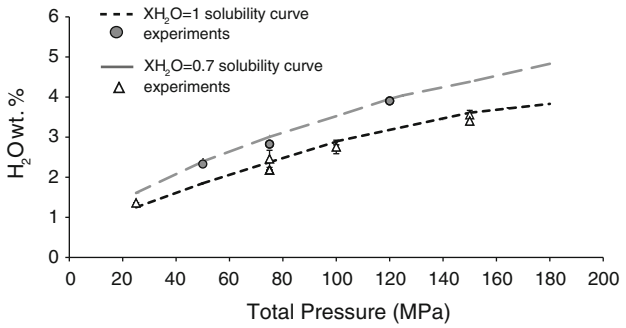

Fig. 7 Total dissolved water concentration in select experimental glasses, measured using FTIR. The FTIR analyses compare well with the solubility curves, indicating the desired XH_2O was successfully achieved in each experimental series. The *gray circles* represent transmission FTIR analyses of total H_2O in glasses from select glassy $XH_2O = 1$ experiments. The *white triangles* are dissolved water concentration data analyzed from select $XH_2O \sim 0.7$ series experiments. The *gray and black dashed lines* are model dissolved H_2O concentrations calculated using Moore et al. (1998), for XH_2O as listed in Table 2

Table 3 Measured water concentrations (FTIR)

Run	H_2O 5200	OH 4500	H_2O total 5200 + 4500	H_2O total 3550
$XH_2O = 1$				
WD31	3.6 (0.3)	–	–	3.91 (0.01)
WD40	1.3 (0.1)[e]	1.2 (0.1)[e]	2.5 (0.1)[e]	2.31 (0.04)
WD44	1.0 (0.2)	1.8 (0.3)	2.8 (0.4)	–
$XH_2O \sim 0.7$				
WD06	0.8 (0.1)	1.5 (0.3)	2.3 (0.3)	2.6 (0.1)
WD12	1.90 (0.03)	1.6 (0.1)	3.6 (0.1)	–
WD13	1.0 (0.2)	1.2 (0.4)	2.2 (0.4)	–
WD15	0.4 (0.2)	1.0 (0.3)	1.4 (0.4)	1.36 (0.06)
WD16	–	–	–	2.8 (0.2)
WD21	0.86 (0.07)	1.7 (0.3)	2.6 (0.3)	2.2 (0.3)
WD22	1.8(0.1)[e]	1.6 (0.1)[e]	3.4(0.1)[e]	–

[a] $\varepsilon_{5200} = 1.07$ L/mol/cm^{-1} (Fe-bearing andesite; Mandeville et al. 2002)

[b] $\varepsilon_{4500} = 0.79$ L/mol/cm^{-1} (Mandeville et al. 2002)

[c] $e_{3550} = 70.3$ L/mol/cm^{-1} (Mt Hood andesite; King et al. 2002)

[d] Number in parentheses = standard deviation from multiple analyses on the same sample

[e] Error estimated after Mandeville et al. (2002)

Experimental pyroxene

Pyroxenes in both XH_2O series experiments are predominantly clinopyroxene, with two lower P–T runs forming orthopyroxene (Figs. 2, 3, 9; Table 4). The clinopyroxenes are diopside (Wo_{46} En_{40} Fs_{14}) to augite (Wo_{35} En_{42} Fs_{21}), with the $XH_2O = 1$ experiments extending further into the

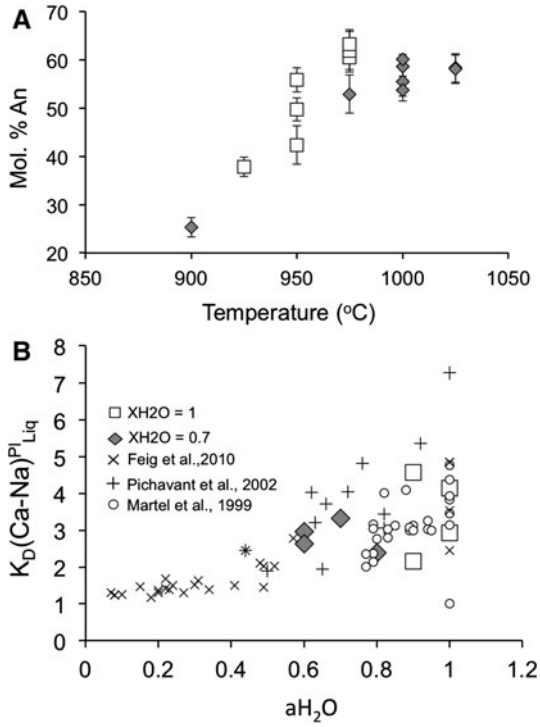

Fig. 8 **a** Experimental plagioclase An content plotted against temperature at pressures of 75–150 MPa, with the majority of data between 90 and 120 MPa. The $XH_2O = 1$ experiments are shown by the *white squares* and the $XH_2O = 0.7$ series by the *gray diamonds* (see legend). *Error bars* represent 1σ about the average An content. **b** Activity of H_2O (aH_2O) plotted against $K_D(Ca-Na)^{pl-liq}$ in comparison with prior studies (Feig et al. 2010; Martel et al. 1999; Pichavant et al. 2002), showing the general increase in plagioclase CaO content with increasing aH_2O. Symbols are described in the legend

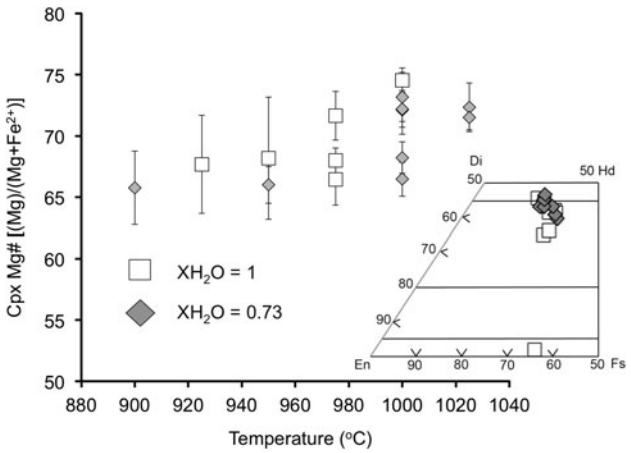

Fig. 9 Clinopyroxene Mg# plotted against experimental temperature. The *symbols* are as explained in the legend. The inset shows the pyroxene quadrilateral for the $XH_2O = 1$ (*white squares*) and $XH_2O \sim 0.7$ (*gray diamonds*) series experiments

augite field than the $XH_2O \sim 0.7$ series (Fig. 10). The orthopyroxene analyzed in experiment WD52 ($XH_2O = 1$) is enstatitic ($Wo_2En_{63}Fs_{35}$; Fig. 9).

Magnesium numbers (Mg#) of the experimental clinopyroxenes, calculated as molar $Mg/(Mg + Fe^{2+})$ with Fe^{2+} estimated stoichiometrically, range between 65 and 75 over both experimental series (Fig. 9). There is no apparent difference between the ranges of Mg# in each XH_2O series, when error bars on Mg# are considered (Fig. 9), but there is a slight increase in Mg# with increasing experimental temperatures.

Discussion

Approach to equilibrium

The assessment of equilibrium in experimental charges is difficult because the timescales needed to achieve complete equilibration of solid phases (plagioclase and pyroxene) are long and at experimental conditions could exceed tens to hundreds of years. Such long timescales are impractical for experimental petrology, so typically achievement of local equilibrium between the newly formed crystals and adjacent melt is deemed sufficient for applying to natural magma systems (e.g., Hirschmann et al. 2008; Pichavant et al. 2007).

The experiments conducted for this study are all of the melting type and we did not run reversal experiments. Of the more than 65 experiments initially run, we filtered out a significant number that showed signs of disequilibrium. The remaining 38 experiments share characteristics that provide evidence for close approach to equilibrium. Texturally, those experiments formed euhedral microphenocrysts with sharp edges in contact with the glass phase. Experimentally grown crystal phases are distributed evenly throughout the charges.

The criteria we used to filter suspect experiments include the following: large standard deviations or inhomogeneity in the phase compositions; run durations that were deemed too short in comparison with prior studies at similar conditions and in generally similar compositions (e.g., Blatter and Carmichael 2001); and/or measured mineral-melt partition coefficients that are far outside those deemed to represent equilibrium, by comparing with prior experimental studies and models (e.g., Putirka 2008; Lange et al. 2009).

Successful experimental durations ranged between 6 and 126 h, with the majority run for at least 48 h (Blatter and Carmichael 2001; Moore and Carmichael 1998). With one exception (24 h, WD56; Table 2), the shortest duration experiments (6–33 h) were reserved for near-liquidus conditions, where the phase assemblage consists of glass or glass + magnetite only. Compared with many phase equilibria studies on similar starting compositions (basalt to andesite) and similar P–T–XH_2O and fO_2 conditions, our run durations are appropriate (e.g., Sisson and Grove 1993a, b; Moore and Carmichael 1998; Blatter and Carmichael 2001; Pichavant et al. 2002; Barclay and Carmichael 2004; Berndt et al. 2005; Di Carlo et al. 2006; Pichavant and Macdonald 2007; Freise et al. 2009; Feig et al. 2010).

About 1/3 of the total number of experiments we ran may not have equilibrated sufficiently. There are two possible reasons for this. In the experimental configuration used (externally heated hydrothermal cold-seal pressure vessels), it is difficult to maintain desired fO_2 conditions for very long run times (>48–100 h) because of hydrogen diffusion from the experimental capsule. A minimum of 48 h is deemed necessary for approach to equilibrium in andesite to basaltic andesite compositions at similar conditions (e.g., Moore and Carmichael 1998), yet significantly longer run times may be needed especially at relatively low P–T conditions. Running experiments longer than 48–100 h introduces potential difficulties of maintaining experimental fluid compositions in mixed H_2O–CO_2 experiments due to possible hydrogen diffusion from the capsule. An improvement in our methods would be to quench and reload the experiments after a suitable amount of time, replenishing the fluids and CH_4 gas to buffer against hydrogen diffusion (e.g., Blatter and Carmichael 2001).

Our experiments employed powdered, natural starting materials, with pre-existing crystals that provide sites for nucleation and encourage phase growth. Prior attempts to run experiments starting with pre-melted and homogenized starting materials proved difficult because the very fine-grained crystal textures that result are very difficult to analyze. Although our experiments are texturally mature, the presence of relict crystal fragments means that only the very outer edge of those crystals equilibrated with the experimental melt. Using the natural powders provided crystals large enough to analyze, yet inconsistencies in phase composition may have resulted from imprecise placement of the electron beam, causing us to discard a number of experiments due to inconsistencies in the phase compositions.

Phase relations

Recent phase equilibria studies on tholeiitic, alkalic, and differentiated MORB basalt starting compositions (e.g., Berndt et al. 2005; Feig et al. 2006; Freise et al. 2009) crystallized magnetite on the liquidus at $XH_2O = 1$ and $fO_2 \sim$ FMQ +2 to +4 log units. Although our starting composition is more silicic, both $XH_2O = 1$ and 0.7 experiments produced Ti-magnetite on the liquidus (Figs. 2, 3, 5). The P–T conditions of the liquidus curves are generally similar within $\sim$10 °C, with the $XH_2O = 1$ liquidus slightly lower in temperature than the

Table 4 Experimental phase compositions

Run	SiO_2	TiO_2	Al_2O_3	$FeOt/Fe_2O_3$	MnO	MgO	CaO	Na_2O	K_2O	Total[c]	Wo An	En Ab	Fs Or	KD[d] FeOt	KD[d] Fe^{2+}
WD03															
Cpx (2)[a]	48.42 (0.76)[b]	1.73 (0.22)	4.22 (0.96)	11.05 (0.53)	0.41 (0.08)	13.31 (0.17)	20.67 (0.01)	–	–	99.79	43	39	19	0.48	0.38
Plag (2)	53.53 (0.43)	–	29.62 (0.19)	0.89 (0.20)	–	0.12 (0.01)	11.04 (0.42)	4.79 (0.34)	0.15 (0.04)	100.15	56	44	1		
Mgt (1)	–	8.6	2.4	86.1	–	2.9	–	–	–	100					
Gl (5)	64.10 (0.25)	1.50 (0.39)	15.41 (0.28)	4.17 (0.25)	0.12 (0.07)	2.13 (0.02)	4.25 (0.15)	5.48 (0.27)	2.03 (0.14)	98.66					
WD05															
Plag (18)	54.51 (0.76)	–	28.79 (0.55)	1.05 (0.16)	–	0.12 (0.03)	10.31 (0.83)	5.23 (0.41)	0.20 (0.04)	100.23	52	47	1		
WD06															
Cpx (2)	49.78 (1.32)	0.98 (0.26)	3.76 (1.05)	9.74 (0.71)	0.35 (0.07)	14.28 (0.70)	21.11 (0.43)	0.39 (0.04)	–	100.39	43	41	16	0.24	0.19
Plag (5)	52.17 (0.94)	–	29.90 (0.58)	1.02 (0.25)	–	0.12 (0.04)	11.61 (0.95)	4.49 (0.28)	0.14 (0.03)	99.45	58	41	1		
Gl (11)	60.90 (0.81)	1.83 (0.78)	15.67 (0.34)	4.79 (0.25)	0.18 (0.06)	2.57 (0.10)	6.14 (0.55)	5.67 (0.23)	1.64 (0.09)	97.43					
WD10															
Gl (34)	56.84 (0.44)	1.71 (0.21)	16.33 (0.42)	7.35 (0.26)	0.19 (0.07)	3.59 (0.09)	7.18 (0.46)	5.03 (0.23)	1.21 (0.09)	97.17					
WD12															
Cpx (4)	47.51 (0.69)	1.41 (0.21)	5.01 (0.82)	11.84 (0.35)	0.33 (0.07)	13.16 (0.47)	19.13 (0.39)	–	–	98.41	41	39	20	0.34	0.28
Plag (5)	53.16 (1.06)	–	27.91 (0.95)	1.13 (0.25)	–	0.15 (0.13)	12.43 (0.34)	4.43 (0.05)	0.17 (0.09)	99.55	60	39	1		
Mgt (1)	4.6	1.9	3	83.4	–	4.9	1.8	–	–	100					
Gl (30)	63.3 (0.4)	1.1 (0.2)	17.2 (0.2)	3.3 (0.2)	0.13 (0.05)	1.75 (0.08)	4.8 (0.2)	5.7 (0.3)	2.0 (0.1)	95.11					
WD13															
Gl (10)	56.77 (0.36)	2.23 (0.50)	15.61 (0.30)	6.52 (0.29)	0.2 (0.1)	3.27 (0.08)	8.33 (0.45)	5.19 (0.21)	1.33 (0.07)	96.86					
WD15															
Gl (8)	55.37 (0.56)	1.93 (0.58)	15.57 (0.17)	9.22 (0.28)	0.18 (0.04)	3.58 (0.11)	7.38 (0.69)	4.99 (0.26)	1.23 (0.10)	98.58					
WD16															
Gl (11)	58.20 (0.66)	1.57 (0.36)	16.78 (0.22)	6.04 (0.24)	0.16 (0.05)	3.08 (0.13)	7.48 (0.24)	4.73 (0.21)	1.40 (0.10)	95.53					
WD18															
Cpx (6)	48.77 (0.52))	1.12 (0.22)	3.63 (0.51)	10.01 (0.48)	0.32 (0.04)	14.08 (0.41)	20.78 (0.42)	0.40 (0.04)	–	99.13	43	41	17	0.26	0.19
Plag (12)	52.65 (0.5)	–	29.14 (0.3)	1.15 (0.2)	–	0.27 (0.03)	11.40 (0.70)	4.40 (0.24)	0.22 (0.11)	99.30	58	41	1		
Gl (9)	59.59 (0.48)	1.85 (0.32)	17.20 (0.31)	4.86 (0.15)	0.16 (0.03)	2.77 (0.09)	5.6 (0.36)	5.7 (0.16)	1.54 (0.08)	97.14					
WD20															
Plag (12)	53.23 (0.98)	–	29.07 (0.78)	1.43 (0.15)	–	0.14 (0.06)	10.51 (0.86)	5.05 (0.5)[c]	0.17 (0.06)	99.62	53	46	1		
WD21															
Gl (34)	55.48 (0.60)	2.23 (0.29)	15.71 (0.30)	8.28 (0.89)	0.22 (0.05)	3.50 (0.14)	7.98 (0.28)	4.79 (0.24)	1.23 (0.09)	97.99					
WD22															
Gl (9)	58.39 (0.29)	1.04 (0.32)	17.39 (0.24)	3.95 (0.19)	0.17 (0.04)	3.22 (0.09)	8.37 (0.18)	5.42 (0.18)	1.43 (0.10)	96.51					

Table 4 continued

Run	SiO_2	TiO_2	Al_2O_3	$FeOt/Fe_2O_3$	MnO	MgO	CaO	Na_2O	K_2O	Total[c]	Wo An	En Ab	Fs Or	KD[d] FeOt	KD[d] Fe^{2+}
WD24															
Cpx (10)	50.25 (0.61)	0.72 (0.17)	2.75 (0.72)	9.26 (0.56)	0.33 (0.07)	14.17 (0.48)	20.52 (0.57)	0.32 (0.04)	–	98.33	43	41	16	0.43	0.41
Gl (15)	59.37 (0.42)	1.46 (0.31)	18.73 (0.29)	4.02 (0.15)	0.15 (0.05)	2.39 (0.09)	6.41 (0.40)	5.47 (0.29)	1.40 (0.1)	97.08					
WD27															
Cpx (3)	49.13 (1.32)	1.65 (0.16)	4.09 (0.29)	12.65 (0.94)	0.42 (0.07)	13.63 (0.67)	19.03 (0.34)	–	–	100.62	40	39	21		
Plag (5)	53.64 (0.94)	–	29.29 (0.64)	0.99 (0.05)	–	0.12 (0.03)	11.13 (0.92)	4.83 (0.41)	0.19 (0.03)	100.21	55	43	1		
WD28															
Gl (7)	58.63 (0.21)	1.10 (0.14)	16.31 (0.25)	4.97 (0.23)	0.2 (0.03)	3.45 (0.13)	8.00 (0.14)	5.38 (0.21)	1.41 (0.06)	95.56					
WD29															
Gl (35)	56.41 (0.53)	1.95 (0.33)	16.16 (0.20)	8.19 (0.37)	0.16 (0.05)	3.51 (0.13)	7.10 (0.32)	4.74 (0.37)	1.23 (0.11)	98.45					
WD30															
Cpx (7)	47.94 (0.51)	1.38 (0.14)	4.43 (0.45)	11.79 (0.60)	0.33 (0.02)	12.88 (0.29)	20.23 (0.49)	–	–	99.01	42	37	19		
Plag (7)	54.13 (0.55)	–	29.53 (0.27)	0.82 (0.14)	–	0.12 (0.02)	11.02 (0.57)	4.70 (0.20)	0.17 (0.02)	100.49	56	43	1		
WD31															
Cpx (10)	48.45 (0.54)	1.34 (0.23)	4.56 (0.39)	11.92 (0.36)	0.33 (0.07)	13.23 (0.26)	19.88 (0.44)	0.41 (0.06)	–	100.12	42	39	20	0.37	0.30
Plag (9)	52.42 (0.4)	–	29.07 (0.4)	1.10 (0.29)	–	0.14 (0.07)	12.47 (0.97)	4.41 (0.31)	0.13 (0.06)	99.76	61	39	1		
Gl (13)	60.1 (0.7)	1.5 (0.3)	18.3 (0.3)	4.1 (0.1)	0.12 (0.04)	2.3 (0.2)	5.6 (0.5)	5.8 (0.2)	1.5 (0.1)	97.27					
WD35															
Cpx (6)	47.77 (0.41)	1.40 (0.26)	5.16 (0.67)	11.03 (0.23)	0.29 (0.04)	13.14 (0.23)	20.11 (0.62)	–	–	98.94	42	38	18		
Plag (8)	51.83 (1.10)	–	29.58 (1.67)	0.88 (0.22)	–	0.10 (0.03)	12.77 (0.88)	4.24 (0.38)	0.14 (0.06)	99.56	62	37	1		
WD40															
Gl (12)	57.81 (0.52)	1.84 (0.42)	16.73 (0.16)	6.19 (0.20)	0.2 (0.1)	3.21 (0.15)	7.65 (0.32)	4.43 (0.36)	1.32 (0.07)	95.94					
WD41															
Gl (13)	57.37 (0.78)	1.57 (0.32)	16.79 (0.20)	7.51 (0.53)	0.15 (0.05)	3.44 (0.15)	6.80 (0.37)	4.52 (0.12)	1.30 (0.09)	94.70					
WD42															
Gl (15)	58.21 (0.40)	1.51 (0.24)	16.86 (0.20)	5.71 (0.18)	0.14 (0.04)	3.13 (0.12)	8.03 (0.24)	4.52 (0.23)	1.32 (0.10)	96.24					
WD44															
Gl (7)	56.76 (0.24)	2.05 (0.54)	15.70 (0.14)	6.86 (0.23)	0.16 (0.06)	3.46 (0.07)	7.84 (0.69)	5.34 (0.23)	1.32 (0.09)	96.52					
WD47															
Cpx (6)	48.80 (1.26)	1.64 (0.36)	4.39 (0.93)	8.59 (0.36)	0.25 (0.06)	14.11 (0.44)	22.20 (0.62)	0.31 (0.07)	–	100.31	46	40	14	0.29	0.20
Gl (12)	61.72 (0.34)	1.11 (0.25)	17.12 (0.22)	3.87 (0.18)	0.18 (0.04)	2.53 (0.12)	6.29 (0.39)	4.98 (0.27)	1.50 (0.08)	96.90					
WD51															
Cpx (3)	50.58 (0.71)	1.36 (0.19)	3.05 (0.80)	12.31 (2.02)	0.60 (0.11)	14.79 (0.96)	17.02 (0.60)	0.59 (0.13)	–	100.32	35	42	21	0.38	0.38
Plag (5)	56.2 (1.3)	–	27.79 (0.91)	0.96 (0.14)	–	0.15 (0.06)	8.43 (0.83)	6.17 (0.51)	0.25 (0.02)	100.38	42	53	1		
Gl (5)	66.98 (0.40)	0.48 (0.22)	16.37 (0.23)	2.36 (0.04)	0.12 (0.03)	1.33 (0.05)	2.83 (0.04)	6.59 (0.33)	2.41 (0.13)	96.63					

Table 4 continued

Run	SiO_2	TiO_2	Al_2O_3	$FeOt/Fe_2O_3$	MnO	MgO	CaO	Na_2O	K_2O	Total[c]	Wo An	En Ab	Fs Or	KD[d] FeOt	KD[d] Fe^{2+}
[e]Mgt (1)	2.7	14.1	1.2	79.4	0.6	1.5	0.7	–	–	100					
WD52															
Cpx (3)	50.95 (0.65)	0.81 (0.20)	2.29 (1.27)	12.64 (1.48)	0.44 (0.10)	14.84 (1.73)	17.67 (1.39)	0.51 (0.08)	–	100.19	36	43	21	0.39	0.29
Plag (5)	58.2 (1.2)	–	24.2 (2.7)	1.45 (0.15)	–	0.18 (0.09)	7.02 (0.44)	5.86 (0.09)	0.78 (0.28)	101.18	38	57	5		
[e]Opx (1)	45.7	–	3.3	24.3	1.2	24.3	1.2	–	–	100	2	63	35		
Gl (9)	69.34 (0.51)	0.50 (0.32)	15.35 (0.16)	1.67 (0.29)	0.06 (0.05)	0.88 (0.06)	1.82 (0.22)	6.08 (0.35)	2.58 (0.13)	96.06					
WD55															
Mgt (1)	2.4	3.1	3.4	86.7	–	4.3	–	–	–	100					
WD56															
Mgt (1)	2.5	8.46	–	89.1	–	–	–	–	–	100					
WD57															
Plag (4)	54.27 (0.54)	–	29.03 (0.48)	0.85 (0.05)	–	0.11 (0.02)	11.15 (0.05)	5.15 (0.08)	0.18 (0.01)	100.75	54	45	1		
Mgt (1)	2.7	16	–	78.2	–	3.1	–	–	–	100					
WD58															
Mgt (1)	3.8	9.4	2.2	81.84	–	2.73	–	–	–	100					
WD61															
Cpx (8)	47.92 (0.60)	1.31 (0.21)	4.56 (0.36)	11.24 (0.59)	0.29 (0.07)	13.30 (0.24)	20.11 (0.50)	–	–	98.75	42	38	18		
Plag (8)	54.69 (0.97)	–	27.83 (1.18)	1.12 (0.17)	–	0.13 (0.04)	10.23 (0.82)	5.52 (0.31)	0.27 (0.05)	99.67	50	49	2		
WD62															
Cpx (6)	49.36 (0.49)	0.99 (0.14)	4.10 (0.24)	9.48 (0.54)	0.28 (0.07)	13.44 (0.28)	20.67 (0.45)	0.44 (0.07)	–	98.79	44	40	16	0.34	0.33
Plag (8)	51.25 (0.65)	–	29.9 (1.2)	0.91 (0.35)	–	0.4 (0.4)	12.73 (0.61)	4.02 (0.28)	0.02 (0.02)	99.37	63	36	1		
Gl (14)	61.57 (0.58)	1.18 (0.23)	18.31 (0.34)	3.58 (0.15)	0.1 (0.05)	1.90 (0.16)	4.77 (0.35)	6.25 (0.37)	1.74 (0.11)	96.90					
WDL_12															
Plag (3)	53.94 (0.72)	–	28.16 (0.83)	1.28 (0.36)	–	0.4 (0.2)	10.00 (0.71)	4.87 (0.39)	0.28 (0.05)	98.89	52	46	2		
Gl (36)	55.05 (1.00)	3.35 (0.54)	12.45 (0.28)	14.98 (1.00)	0.24 (0.04)	2.22 (0.10)	5.68 (0.27)	4.01 (0.26)	2.00 (0.19)	99.69					

[a] Number of analyses

[b] 1σ standard deviations are in parentheses under each analysis

[c] Glass analyses normalized 100 % volatile free, with original totals reported

[d] Apparent $Kd^{Fe-Mg}_{cpx-liq}$ calculated as FeOt (KD FeOt) and with Fe^{2+} (KD Fe^{2+}) estimated by stoichiometry (Droop 1987)

[e] Magnetite and orthopyroxene analyses reported all FeO as Fe_2O_3 and were analyzed using Energy Dispersive Spectra (EDS)

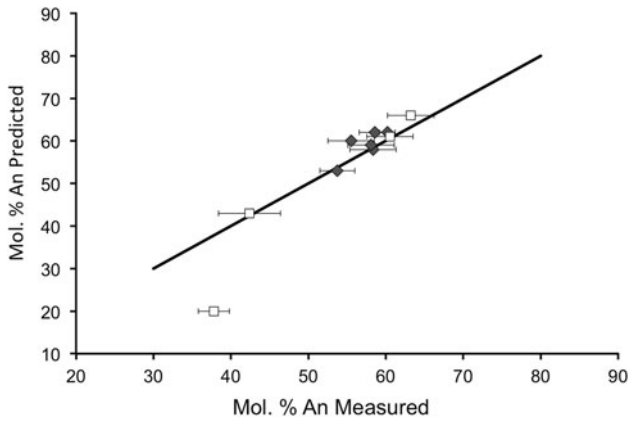

Fig. 10 Plagioclase An contents measured from the experiments plotted against An contents predicted using the model of Lange et al. (2009). We estimated the predicted An contents by using the experimental glass compositions and temperatures and modeling the predicted An content as a function of melt H_2O. We used the predicted An content for the condition that the melt H_2O content used in the model agrees with that either measured or modeled using Moore et al. (1998)

$XH_2O \sim 0.7$ series at similar pressures (Fig. 5). Thus, a modest reduction in XH_2O only slightly influences the position of the liquidus in low MgO basaltic andesite.

In comparison, prior experimental studies using andesite compositions (Blatter and Carmichael 2001; Eggler 1972; Eggler and Burnham 1973; Hammer et al. 2002; Moore and Carmichael 1998) produced plagioclase and/or orthopyroxene on the liquidus, depending on PH_2O. Basaltic andesite from western Mexico produced Cr-spinel and olivine on the liquidus, at $XH_2O = 1$ with $fO_2 \sim$ NNO + 1–2 log units, followed by augitic pyroxene and plagioclase at lower temperatures (Moore and Carmichael 1998).

The low MgO Westdahl basaltic andesite liquidus phase relations compare best with basalts, and the dissimilarities with the prior studies may be explained by the relative concentrations of FeOt and MgO in the different bulk compositions. The Westdahl MW98-16 starting material is significantly higher in FeOt compared with the other experimental studies we considered (Blatter and Carmichael 2001; Eggler 1972; Eggler and Burnham 1973; Hammer et al. 2002; Moore and Carmichael 1998). MW98-16 has 10.82 wt.% FeOt, and when paired with the low MgO (3.29 wt.%), FeOt/MgO is approximately 3.3. In contrast, andesite and basaltic andesite comparison studies have FeOt between 4.3 (Eggler 1972) and 7.1 wt.% (Hammer et al. 2002), yielding FeOt/MgO of 1.1 to 1.9, respectively. The Westdahl starting composition has 1.7 to 3 times higher FeOt/MgO, which could stabilize Ti-magnetite on the liquidus preferential to Mg-rich olivine, orthopyroxene, or Cr-spinel.

In our experiments, clinopyroxene is the second phase to crystallize, forming at similar conditions in both $XH_2O = 1$ and 0.7 experiments (Figs. 2, 3, 5). Clinopyroxene stability is not as dependent on water as plagioclase or amphibole, and thus, it is not expected to show large differences between the $XH_2O = 1$ and 0.7 experiments. In contrast, the relatively low temperature stability of orthopyroxene observed in our experiments has been attributed by prior studies to high water content preferentially stabilizing clinopyroxene (Feig et al. 2006; Hamada and Fujii 2008) and the early crystallization of plagioclase (Moore and Carmichael 1998).

The plagioclase stability curve changed the most due to the relatively modest differences in fluid composition at $XH_2O = 1$ and 0.7, because its stability and composition depends on H_2O and T (e.g., Housh and Luhr 1991; Lange et al. 2009; Almeev et al. 2012). Thus, the stability curve is shifted approximately 25 °C to lower temperatures at lower dissolved total H_2O in the melt in the $XH_2O = 1$ series compared with $XH_2O \sim 0.7$ (Fig. 5).

Amphibole stability in the Westdahl basaltic andesite composition is generally similar to prior experiments on water saturated basalts, andesites, and basaltic andesites with $fO_2 \sim$ FMQ + 1–2 log units (Baker and Eggler 1983; Blatter and Carmichael 2001; Eggler 1972; Eggler and Burnham 1973; Freise et al. 2009; Hammer et al. 2002; Moore and Carmichael 1998). Amphibole (H_2O-bearing) requires a minimum meltwater concentration to be stable, and it forms typically at pressures above 100 MPa in experiments with $XH_2O = 1$ in dacites and andesites (e.g., Browne and Gardner 2006). In basalts and basaltic andesites, Na_2O greater than 3 wt.% is required to stabilize pargasitic amphibole at the expense of olivine, when temperatures are low enough that the coexisting liquid is andesitic (Sisson and Grove 1993a). Consistent with those results, amphibole appears in the Westdahl $XH_2O = 1$ series (bulk $Na_2O > 3$ wt.%) at temperatures and pressures >100 MPa at ~900–950 °C and increasing to ~160 MPa at 1,000 °C.

Two possible differences are observed in amphibole stability between the $XH_2O = 1$ and 0.7 series. The minimum pressure stability of amphibole in the $XH_2O \sim 0.7$ experiments appears to increase slightly to ~110 MPa at 900 to 1,000 °C, although additional experiments are required to assess this more precisely. Also, there is a ~10–25 °C increase in the temperature stability limit of amphibole in experiments with >3 wt.% H_2O (Fig. 5), indicating that decreasing XH_2O could modestly influence the upper temperature stability of amphibole at our experimental conditions.

We did not find conclusive evidence for equilibrium olivine crystallizing in any of the Westdahl experiments at $fO_2 \sim$ Ni–NiO and $XH_2O = 0.7$ to 1, except for those run at 0.1 MPa (Table 2). Because our results are more similar to basalt than andesite phase equilibria, we compare with

other studies that did not produce olivine in basaltic starting compositions to explain our findings. Experiments conducted on Izu-Bonin-Mariana (IBM) arc basalt under oxidizing conditions (FMQ +0.6 to 5 log units, MnO-Mn3O4; Tatsumi and Suzuki 2009) failed to produce olivine at any pressure or temperature. The experiments of Berndt et al. (2005) produced olivine on the liquidus in primitive MORB (FeOt/MgO = 0.88) at all water concentrations, but olivine does not crystallize in experiments on a differentiated MORB composition (FeOt/MgO = 1.65), which also produced magnetite on the liquidus. Freise et al. (2009) showed that at oxidizing conditions (ΔFMQ +1 to 4), olivine either did not form or had a stability field reduced to the driest experiments and that magnetite formed on the liquidus in a starting composition with FeOt/MgO = 1.61. At reducing conditions, they observed olivine as a lower temperature phase in tholeiitic basalt, and as the liquidus phase in alkalic basalt, and magnetite did not crystallize at any condition.

The combined observations from those studies (Berndt et al. 2005; Feig et al. 2006, 2010; Freise et al. 2009; Tatsumi and Suzuki 2009) and our own results indicate that oxidizing conditions ($fO_2 \sim$ NNO and higher) and higher water concentrations ($H_2O > 0.6$–1 wt.%) combined tend to produce magnetite as the liquidus phase, and concurrently, the olivine stability field is either absent or confined to lower temperatures. It is possible that this results from a higher proportion of Fe^{3+} in the melt under oxidizing conditions, which could favor formation of magnetite with significant Fe^{3+} in the structure over olivine (predominantly Fe^{2+}). In the low MgO (3.29 wt.%) Westdahl composition, the absence of olivine in the experiments could also signify that the low bulk MgO also influences the lack of olivine found at our experimental conditions.

Variations in plagioclase composition and K_D

Plagioclase compositions increase in An content with increasing water content and temperature (e.g., Hammer et al. 2002; Housh and Luhr 1991; Lange et al. 2009). When plotted as a function of temperature over a relatively restricted range in pressure (Fig. 8a; 90 and 120 MPa), our experimental plagioclase compositions range from $\sim An_{25}$ to $An_{58–62}$ at temperatures from 900 to 1,025 °C, with little difference between experiments at $XH_2O = 1$ and 0.7. Lower temperature experiments produced evolved melts with lower CaO and higher Na_2O and reduced plagioclase An content, while higher temperature experiments produced higher An content plagioclase because of the less evolved melt (higher CaO, lower Na_2O) from which they formed.

Meltwater content exerts a strong control on plagioclase compositions, through the influence of hydroxyl groups on the activities of An and Ab components in the liquid (Lange et al. 2009). A number of experimental studies show this influence by plotting PH_2O versus plagioclase An content at fixed temperature to isolate the effect of water content on plagioclase composition (e.g., Hammer et al. 2002). Because our experiments were run at a range of P–T conditions, it was not possible to show clear trends of plagioclase An content as a function of pressure at a fixed temperature. Thus, we plotted plagioclase $K_D(Ca-Na)^{pl-liq}$ against the estimated activity of water (aH_2O; Burnham 1979) and compare with select prior studies on basalt to andesite compositions at a range of aH_2O (Feig et al. 2010; Martel et al. 1999; Pichavant et al. 2002). All studies combined show an approximate trend of increasing $K_D(Ca-Na)^{pl-liq}$ as a function of increasing aH_2O, as expected, although our results and those of Feig et al. (2010) and Martel et al. (1999) are scattered to low $K_D(Ca-Na)^{pl-liq}$ at aH_2O above ~ 0.8. Perhaps the scatter is a result of variations in the other melt components between the different studies (SiO_2, Al_2O_3, FeO, and MgO; Lange et al. 2009), influencing equilibrium plagioclase compositions.

We also compared the experimental plagioclase compositions with the model of Lange et al. (2009) as a way to gauge consistency with the large number of studies used to calibrate the model. Figure 10 shows all experiments where we analyzed both plagioclase and co-existing glass, using water contents measured either by FTIR or estimated using the model of Moore et al. (1998) from the experimental glass compositions (Fig. 5 caption). The experimental and model predicted plagioclase compositions agree within error for the majority of the experiments from both $XH_2O = 1$ and ~ 0.7 series. The lowest An data point estimated from the model (An_{38}; WD52) lies below the 1:1 line (Fig. 10). This experiment has the most silicic glass composition (70.6 ± 0.7 wt.%), and the number of experiments calibrating the Lange et al. (2009) are sparse for glass compositions >72 wt.% SiO_2. Although WD52 is relatively uniform in glass (±0.7 wt.% SiO_2) and plagioclase (An38 ± 2 mol%) compositions, it has $K_D(Ab-An)^{pl-liq}$ (Putirka 2008) that is slightly lower than the acceptable range. It is possible that both the model results are inaccurate and the plagioclase composition did not fully equilibrate in WD52.

Variations in clinopyroxene apparent K_D

Clinopyroxene–glass pairs in our experiments have calculated ratios of molar Fe^{2+}/Mg (apparent $Kd^{Fe-Mg}_{Cpx-Liq}$) that fall between 0.19 and 0.41, with the average = 0.30 ± 0.08, with Fe^{2+} in the clinopyroxene estimated stoichiometrically

(e.g., Droop 1987) and in the liquid estimated after Ghiorso and Sack (1995). Assuming all Fe as FeO in the clinopyroxene, our range of apparent $Kd^{Fe-Mg}_{cpx-liq}$ rises slightly to 0.35 ± 0.07. In comparison, the accepted equilibrium $Kd^{Fe-Mg}_{cpx-liq}$ cited by Putirka (2008) is 0.28 ± 0.08, derived from a range (0.04 to 0.68; Putirka, 2008) from many reported experimental estimates. Although our experimental *Kd*'s are slightly higher than the published average (although within error), we note that $Kd^{Fe-Mg}_{cpx-liq}$ estimated from prior studies on basalt to andesite are not dissimilar to ours. One possible explanation for the slightly higher average apparent *Kd* from our experiments is the very low MgO in the bulk starting composition. Our experimental melts evolve from 3.29 wt.% in the starting composition to <1 wt.% at ~72 wt.% SiO_2. It is possible that the low melt MgO contents in our experiments shifted the pyroxene compositions to relatively higher FeO at similar SiO_2 when compared with prior studies with lower starting FeOt/MgO.

In comparison, prior experimental results (derived from LEPR; Hirschmann et al. 2008) from select basalt to andesite comparison studies extend broadly between ~0.14 to ~0.57 with individual ranges as follows: 0.27–0.48 for high silica andesite (Blatter and Carmichael 2001); 0.14–0.48 for Mexican basaltic andesite and andesite at pressures >0.1 MPa (Moore and Carmichael 1998); 0.21–0.35 for high-alumina and low MgO basalts (Sisson and Grove 1993a, b); 0.25–0.57 for tholeiitic basalt (Feig et al. 2006); 0.15–0.45 for high-alumina Aleutian basalt (Baker and Eggler 1983); 0.23 ± 0.03 (tholeiitic basalt) and 0.41 ± 0.07 (alkalic basalt; Freise et al. 2009). As noted by Pichavant et al. (2002), increasing proportion of Fe^{3+} in the pyroxene, which is expected with increasing fO_2, would cause the apparent $Kd^{Fe-Mg}_{cpx-liq}$ to rise if calculated assuming all Fe as FeO.

Factors that could cause deviations in apparent $Kd^{Fe-Mg}_{cpx-liq}$ away from the 0.28 ± 0.08 accepted value include bulk compositional differences (e.g., Freise et al. 2009), inhomogeneity in clinopyroxene composition as it crystallizes under disequilibrium conditions initially imposed in the experiments (Mollo et al. 2010), and ranges in experimental fO_2 (Pichavant et al. 2002) Further, Putirka (2008) shows that clinopyroxene with apparently equilibrium *Kd* can in fact result from disequilibrium at high undercoolings. Thus, the criteria of using a fixed value of $Kd^{Fe-Mg}_{cpx-liq}$ may not be the best tool to use on its own to assess the achievement of equilibrium in experiments.

The influence of H_2O and fO_2 on experimental melt evolution

Many recent experimental studies examine how the FeOt/MgO ratio changes in melts as they evolve during equilibrium crystallization, typically starting from a variety of basalt compositions (e.g., Berndt et al. 2005; Feig et al. 2006, 2010; Freise et al. 2009; Pichavant et al. 2002; Sisson and Grove 1993a, b; Sisson et al. 2005; Tatsumi and Suzuki 2009). The two primary influences identified are as follows: (1) H_2O concentration in the experimental fluid; and (2) oxygen fugacity.

Our experiments predict that equilibrium crystallization at ~NNO and $XH_2O = 0.7$ to 1 of a tholeiitic basaltic andesite magma with a high starting FeOt/MgO will produce evolved liquids that first decrease and then remain relatively constant in FeOt/MgO as SiO_2 increases to >70 wt.% with increased crystallization (Fig. 11). High water concentrations suppress early plagioclase crystallization, increasing the proportion of ferromagnesian silicate minerals and leading to an initial depletion in FeOt relative to MgO, which levels off as melt SiO_2 continues to rise (Figs. 11, 12). Stronger depletion of the melt in FeOt, relative to modestly decreasing MgO (Fig. 6), during the early stages of crystallization results from the formation of liquidus Ti-magnetite. The low MgO in the starting composition inhibits crystallization of MgO-rich olivine, which enhances the trend toward reduced melt FeOt/MgO. Our experiments also show a strong trend toward relatively alkali-rich melts and away from FeOt and MgO probably resulting from early crystallization of Fe and Mg-rich Ti-magnetite and clinopyroxene, relative to plagioclase (Fig. 11).

In comparison with select prior studies starting with tholeiitic basaltic compositions (Fig. 12), our results consistently show that experiments with higher melt H_2O contents (>1 wt.%; e.g., Tatsumi and Suzuki 2009) and higher fO_2 trend more strongly toward calc-alkaline melt compositions (Irvine and Baragar 1971). Hamada and Fujii (2008) studied tholeiitic basalt with 3–4.4. wt.% H_2O and predict a trend toward calc-alkaline melts, enrichment in alkalis with depletion in FeOt and MgO, similar to our study and Tatsumi and Suzuki (2009), although their starting composition is high MgO (13 wt.%; FeOt/MgO = 0.81.), and Westdahl is only ~3.5 wt.% MgO and IBM is ~6.5 wt.% MgO. Their experiments do not evolve very far from the starting composition when plotted on the AFM diagram, though they include projected evolution trends. Experiments on basalt under very oxidized conditions of NNO +4 log units caused the evolving melts to decrease in FeOt/MgO (e.g., Sisson et al. 2005; Tatsumi and Suzuki 2009), becoming calc-alkaline (Miyashiro 1974).

In contrast, Feig et al. (2006, 2010) observed FeOt enrichment as MgO initially decreased at >0.6 wt.% H_2O. Although their liquids remain in the calc-alkaline field in the AFM diagram, their compositional evolution is very different than either the Westdahl or IBM studies (Fig. 12; Tatsumi

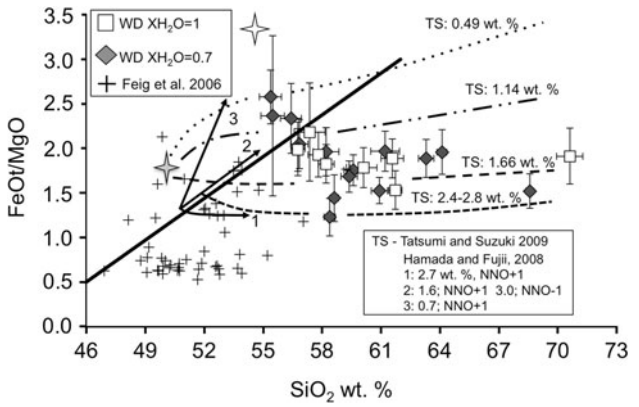

Fig. 11 Calculated ratio of FeOt/MgO versus SiO_2 wt.% from the experimental glasses. The *white squares* represent $XH_2O = 1$ series glasses and the *gray diamonds* represent the $XH_2O \sim 0.7$ experiments. The *white star* represents the bulk rock FeOt/MgO of the starting material. The *solid line* is the discrimination between tholeiitic and calc-alkaline fields (Miyashiro 1974). The *dashed line* traces the trend of natural Westdahl magma compositions, which are strongly tholeiitic according to Miyashiro (1974)

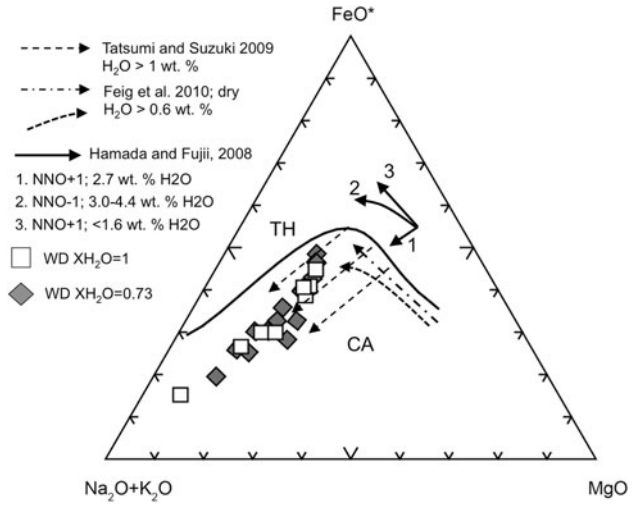

Fig. 12 AFM diagram after Irvine and Baragar (1971) showing our experiments deviating from the tholeiitic region of the diagram, despite a highly tholeiitic starting material. The addition of water and a high fO_2 caused the experiments to follow a calc-alkaline evolution, similar to what other researchers have found using less tholeiitic starting materials but similar oxidizing conditions. The *black line* denotes the boundary between tholeiitic and calc-alkaline fields. The *white squares* are the $XH_2O = 1$ experimental glass compositions projected onto the AFM diagram, using the model IgPet by Michael Carr. The *gray diamonds* are the $XH_2O \sim 0.7$ series experiment glass compositions. The dashed black lines are representative experimental melt compositions from Tatsumi and Suzuki (2009) and Feig et al. (2010) showing examples of basalt experiments producing calc-alkaline trends at high water contents and $fO_2 \sim$ FMQ + 2 log units and tholeiitic trends at low water concentrations and reducing fO_2 (FMQ)

and Suzuki 2009). They start with FeOt/MgO = 0.64, high MgO (10.2), lower FeOt = 6.5 microgabbro and find Cr-spinel and olivine on the liquidus. The initial depletion in MgO as FeOt increases is most likely due to higher proportions of olivine, relative to plagioclase and Fe–Ti oxides, as crystallization proceeds away from the liquidus.

Low H_2O content (<1–1.6 wt %) experiments behave differently and typically trend toward tholeiitic compositions (Hamada and Fujii 2008; Tatsumi and Suzuki 2009), particularly at lower fO_2 (FMQ; Feig et al. 2010). In those experiments, early crystallization of olivine drives the melt to increase in FeOt/MgO with depletion in MgO as crystallization starts. Reduced fO_2 causes the melt to evolve to higher FeOt/MgO relative to oxidized conditions (Fig. 11; Freise et al. 2009; Hamada and Fujii 2008; Minitti and Rutherford 2000; Sisson et al. 2005; Tatsumi and Suzuki 2009). Reducing the fugacity to NNO + 1 log unit in the same system causes the melt liquid line of descent to shift slightly toward higher FeOt/MgO liquids, toward the tholeiitic field of Miyashiro (1974; Tatsumi and Suzuki 2009). Dry experiments at FMQ show a very strong tholeiitic trend indicating that water may exert greater influence on the FeOt/MgO ratio of the melt, but that the more reducing fO_2 was also important.

When fO_2 is relatively reduced (FMQ or less), Fe–Ti oxide crystallization is suppressed (Freise et al. 2009; Sisson et al. 2005). If accompanied by early crystallization of Mg-rich minerals, the melt would tend to be relatively enriched in FeOt and depleted in MgO, causing a trend of increasing FeOt/MgO as it evolves and SiO_2 increases. In comparing the melt evolution between alkalic and tholeiitic basalt starting compositions, increasing XH2O from 0.2 to 1 had less of an effect (Freise et al. 2009). However, the calc-alkaline trend observed by Freise et al. (2009) shows a continued increase in FeOt/MgO within the calc-alkaline field defined by Miyashiro (1974), while our study predicts that at NNO and $XH_2O = 0.7$–1, the trend should initially decrease and then become constant in FeOt/MgO with increasing SiO_2 (Fig. 11). It is possible that at reducing conditions (<NNO), fO_2 controls the ratio of FeOt/MgO in the melt, while at higher fO_2 (>NNO), H_2O exerts a stronger influence.

Conclusions

Our experiments predict that at oxidized conditions (NNO) and high H_2O concentrations ($XH_2O \sim 0.7$ to 1), crystallizing low MgO basaltic andesite produces melts that follow a calc-alkaline differentiation trend at crustal conditions, using criteria from Miyashiro (1974), Kuno (1968), and Irvine and Baragar (1971). Our experiments also suggest that the starting FeOt/MgO may be important in controlling the liquidus phase, with high FeOt/MgO (greater than ~1) favoring Ti-magnetite on the liquidus at similarly high XH_2O and fO_2 (e.g., Tatsumi and Suzuki

2009). At crustal conditions, basaltic andesite magmas with initially high FeOt/MgO can evolve along a calc-alkaline trend if sufficiently high XH_2O and fO_2 conditions exist locally. Our results agree with other studies on basaltic compositions at similar conditions, showing that tholeiitic basaltic andesite could produce calc-alkaline composition melts at shallow to mid-crustal pressures, thereby influencing the shallow evolution of H_2O-rich arc magmas.

Acknowledgments Work supported by National Science Foundation Grant No. EAR 0636118. We thank Cole Kingsbury and Christina Whitmore for general laboratory assistance and The Murdock Trust for funding the micro-FTIR equipment. We thank Pavel Izbekov, Chris Nye, and Laura Walker for discussions and suggestions that improved the study. This study was greatly improved by thoughtful reviews from Dawnika Blatter, Don Baker, and two anonymous reviewers of a prior version of the manuscript. We thank Kayla Iacovino, Renat Almeev, and an anonymous reviewer for their insightful reviews that helped improve this version of the study. The electron microprobe analyses were collected using the Advanced Instrumentation Laboratory equipment, and we thank Ken Severin for analytical support and assistance.

References

Almeev R, Holtz F, Koepke J, Parat F (2012) Experimental calibration of the effect of H_2O on plagioclase crystallization in basaltic melt at 200 MPa. Am Mineral 97:1234–1240

Annen C, Blundy JD, Sparks RS (2006) The genesis of intermediate and silicic magmas in deep crustal hot zones. J Petrol 47:505–539

Arculus RJ (2003) Use and abuse of the terms calcalkaline and calkalkalic. J Petrol 44:929–935

Asimow PD, Ghiorso MS (1998) Algorithmic modifications extending MELTS to calculate subsolidus phase relations. Am Min 83:1127–1132

Baker DR, Eggler DH (1983) Fractionation paths of Atka (Aleutians) high-alumina basalts: constrains from phase relations. J Volc Geotherm Res 18:387–404

Barclay J, Carmichael ISE (2004) A hornblende basalt from western Mexico; water-saturated phase relations constrain a pressure-temperature window of eruptibility. J Petrol 45:485–506. doi:10.1093/petrology/egg/091

Behrens H, Ohlhorst S, Holtz F, Champenois M (2004) CO_2 solubility in dacitic melts equilibrated with H_2O-CO_2 fluids: implications for modeling the solubility of CO_2 in silicic melts. Geochim Cosmochim Acta 68:4687–4703

Berndt J, Koepke J, Holtz F (2005) An experimental investigation of the influence of water and oxygen fugacity on differentiation of MORB at 200 MPa. J Pet 46:135–167

Blank JG, Brooker RA (1994) Experimental studies of carbon dioxide in silicate melts; solubility, speciation, and stable carbon isotope behavior. Rev Min 30:157–186

Blatter DL, Carmichael ISE (2001) Hydrous phase equilibria of a Mexican high-silica andesite: a candidate for a mantle origin? Geochim Cosmochim Acta 65:4043–4065

Botcharnikov R, Freise M, Holtz F, Behrens H (2005) Solubility of C-O-H mixtures in natural melts: new experimental data and application range of recent models. Ann Geophys 48:633–645

Browne B, Gardner J (2006) The influence of magma ascent path on the texture, mineralogy, and formation of hornblende reaction rims. Earth Planet Sci Lett 246:161–176

Burnham CW (1979) The importance of volatile constituents. In: Yoder HS (ed) The evolution of the igneous rocks. Princeton University Press, New Jersey

Church BN, Johnson WM (1980) Calculation of the refractive index of silicate glasses from chemical composition. Geol Soc Am Bull 91:619–625

Di Carlo I, Pichavant M, Rotoloi S, Scaillet S (2006) Experimental Crystallization of a High-K Arc Basalt: the Golden Pumice, Stromboli Volcano (Italy). J Petrol 47:1317–1343

Droop GTR (1987) A general equation for estimating Fe^{3+} concentrations in ferromagnesian silicates and oxides from microprobe analyses, using stoichiometric criteria. Min Mag 51:431–435

Eggler DH (1972) Amphibole stability in H_2O-undersaturated calc-alkaline melts. Earth Planet Sci Lett 15:28–34

Eggler DH, Burnham CW (1973) Crystallization and fractionation trends in the system andesite-H_2O-CO_2-O_2 at pressures to 10 Kb. Geol Soc Am Bull 84:2517–2532

Eichelberger JC, Izbekov PE, Browne BL (2006) Bulk chemical trends at arc volcanoes are not liquid lines of descent. Lithos 87:135–154

Feig ST, Koepke J, Snow JE (2006) Effect of water on tholeiitic basalt phase equilibria: an experimental study under oxidizing conditions. Contrib Mineral Petrol 152:611–638

Feig ST, Koepke J, Snow JE (2010) Effect of oxygen fugacity and water on phase equilibria of a hydrous tholeiitic basalt. Contrib Mineral Petrol. doi:10.1007/s00410-010-0493-3

Freise M, Holtz F, Nowak M, Scoates JS, Strauss H (2009) Differentiation and crystallization conditions of basalts from the Kerguelen large igneous province: an experimental study. Contrib Mineral Petrol 158:505–527

Ghiorso MS, Sack RO (1995) Chemical mass transfer in magmatic processes IV. A revised and internally consistent thermodynamic model for the interpolation and extrapolation of liquid-solid equilibria in magmatic systems at elevated temperatures and pressures. Contrib Mineral Petrol 119:197–212

Grove TL (1981) Use of FePt alloys to eliminate the iron loss problem in 1-atmosphere gas mixing experiments: theoretical and practical considerations. Contrib Mineral Petrol 78:298–304

Grove TL, Baker MB (1984) Phase equilibrium controls on the tholeiitic verses calc- alkaline differentiation trends. J Geophys Res 89:3253–3274

Grove TL, Juster TC (1989) Experimental investigations of low-Ca pyroxene stability and olivine-pyroxene-liquid equilibria at 1-atm in natural basaltic and andesitic liquids. Contrib Mineral Petrol 103:287–305

Hamada M, Fujii T (2008) Experimental constraints on the effects of pressure and H2O on the fractional crystallization of high-Mg island arc basalt. Contrib Mineral Petrol 155:767–790

Hammer JE, Rutherford MJ, Hildreth W (2002) Magma storage prior to the 1912 eruption at Novarupta, Alaska. Contrib Mineral Petrol 144:144–162. doi:10.1007/s00410-002-0393-2

Hirschmann MM, Ghiorso MS, Davis FA, Gordon SM, Mukherjee S, Grove TL, Krawczynski M, Médard E, Till CB (2008) Library of experimental phase relations (LEPR): a database and web portal for experimental magmatic phase equilibria data. Geochem Geophys Geosyst 9(3):Q03011. doi:10.1029/2007GC001894

Holloway JR, Burnham CW, Millhollen GL (1968) Generation of H_2O-CO_2 mixtures for use in hydrothermal experimentation. J Geophys Res 73:6598–6600

Housh TB, Luhr JF (1991) Plagioclase-melt equilibria in hydrous systems. Am Mineral 76:477–492

Irvine TN, Baragar WRA (1971) A guide to the chemical classification of the common volcanic rocks. Can J Earth Sci 8:523–548

Kawamoto T (1996) Experimental constraints on differentiation and H2O abundance of calc-alkaline magmas. Earth Planet Sci Lett 144:577–589

Kawamoto T, Hirose K (1994) Au-Pd sample containers for melting experiments on iron and water bearing systems. Eur J Mineral 6:381–385

Kay S, Kay R, Citron G (1982) Tectonic controls on tholeiitic and calc-alkaline magmatism in the Aleutian Arc. J Geophys Res 87:4051. doi:10.1029/JB087iB05p04051

Kelley K, Plank T, Grove T, Stolper E, Newman S, Hauri E (2006) Mantle melting as a function of water content beneath back-arc basins. J Geophys Res 111:27. doi:10.1029/2005JB003732

King PL, Vennemann TW, Holloway JR, Hervig RL, Lowenstern JB, Forneris JF (2002) Analytical techniques for volatiles: a case study using intermediate (andesitic) glasses. Am Mineral 87:1077–1089

Kuno H (1968) Petrology of Hakone Volcano and adjacent areas. Geol Soc Am Bull 61:957–1020

Lange RA, Carmichael ISE (1987) Densities of Na_2O-K_2O-CaO-MgO-FeO-Fe_2O_3-Al_2O_3-TiO_2-SiO_2 liquids: new measurements and derived partial molar properties. Geochim Cosmochim Acta 51:2931–2946

Lange RA, Frey HM, Hector J (2009) A thermodynamic model for the plagioclase-liquid hygrometer/thermometer. Am Mineral 94: 494–506

Mandeville CW, Webster JD, Rutherford MJ, Taylor BE, Timbal A, Faure K (2002) Determination of molar absorptivities for infrared absorption bands of H_2O in andesitic glasses. Am Mineral 87:813–821

Martel C, Pichavant M, Holtz F, Scaillet B, Bourdier JL, Traineau H (1999) Effects of fO_2 and H_2O on andesite phase relations between 2 and 4 kbar. J Geophys Res 104:29453–29470

Minitti ME, Rutherford MJ (2000) Genesis of the Mars Pathfinder "sulfur-free" rock from SNC parental liquids. Geochim Cosmochim Acta 64:2535–2547

Miyashiro A (1974) Volcanic rock series in island arcs and active continental margins. Am J Sci 274:321–355

Mollo S, Del Gaudio P, Ventura G, Iezzi G, Scarlato P (2010) Dependence of clinopyroxene composition on cooling rate in basaltic magmas: implications for thermobarometry. Lithos 118:302–312

Moore G, Carmichael ISE (1998) The hydrous phase equilibria (to 3 kbar) of an andesite and basaltic andesite from western Mexico: constrains on water content and conditions of phenocryst growth. Contrib Mineral Petrol 130:304–319

Moore G, Vennemann T, Carmichael ISE (1998) An empirical model for the solubility of H_2O in magmas to 3 kilobars. Am Mineral 83:36–42

Morgan GB, London D (1996) Optimizing the electron microprobe analysis of hydrous alkali aluminosilicate glasses. Am Mineral 81:1176–1185

Nichols ARL, Wysoczanski RJ (2007) Using micro-FTIR spectroscopy to measure volatile contents in small and unexposed inclusions hosted in olivine crystals. Chem Geol 242:371–384

Peacock MA (1931) Classification of igneous rocks. J Geol 39:54–67

Pichavant M, Macdonald R (2007) Crystallization of primitive basaltic magmas at crustal pressures and genesis of the calc-alkaline igneous suite: experimental evidence from St Vincent, Lesser Antilles arc. Contrib Mineral Petrol 154:535–558. doi:10.1007/s00410-007-0208-6

Pichavant M, Mysen BO, Macdonald R (2002) Source and H_2O content of high-MgO magmas in island arc settings: an experimental study of a primitive calc-alkaline basalt from St. Vincent, Lesser Antilles arc. Geochim Cosmochim Acta 66: 2193–2209

Pichavant M, Costa F, Burgisser A, Scaillet B, Martel C, Poussineau S (2007) Equilibration scales in silicic to intermediate magmas implications for experimental studies. J Pet 48:1955–1972

Pownceby MI, O'Neill HSC (1994) Thermodynamic data from redox reactions at high temperatures. IV. Calibration of the Re-ReO_2 oxygen buffer from EMF and NiO-Ni-Pd redox sensor measurements. Contrib Mineral Petrol 118:130–137

Putirka KD (2008) Thermometers and barometers for volcanic systems. Rev Mineral Geochem 69:61–120. doi:10.2138/rmg.2008.69.3

Sato M (1971) Electrochemical measurements and control of oxygen fugacity and other gaseous fugacities with solid electrolyte sensors. In: Ulmer GC (ed) Research techniques for high pressure and high temperature, pp 43–99

Scaillet B, Pichavant M, Roux J, Humbert G, Lefevre A (1992) Improvements of the Shaw membrane technique for measurement and control of fH_2 at high temperatures and pressures. Am Mineral 77:647–655

Scaillet B, Pichavant M, Roux J (1995) Experimental crystallization of leucogranite magmas. J Petrol 36:663–705

Shaw HR (1963) Hydrogen-water vapour mixtures: control of hydrothermal experiments by hydrogen osmosis. Science 139: 1220–1222

Sisson TW, Grove TL (1993a) Experimental investigations of the role of H_2O in calc- alkaline differentiation and subduction zone magmatism. Contrib Mineral Petrol 113:143–166

Sisson TW, Grove TL (1993b) Temperatures and H_2O contents of low-MgO high- alumina basalts. Contrib Mineral Petrol 113: 167–184

Sisson TW, Ratajeski K, Hankins WB, Glazner AF (2005) Voluminous granitic magmas from common basaltic sources. Contrib Mineral Petrol 148:635–661

Tatsumi Y, Suzuki T (2009) Tholeiitic vs calc-alkalic differentiation and evolution of arc crust: constraints from melting experiments on a basalt from Izu-Bonin-Mariana arc. J Petrol 50:1575–1603

Tatsumi Y, Sakuyama M, Fukuyama H, Kushiro I (1983) Generation of arc basalt magmas and thermal structure of the mantle wedge in subduction zones. J Geol Res 88:5815–5825

Taylor JR, Wall VJ, Pownceby MI (1992) The calibration and application of accurate redox sensors. Am Mineral 77:284–295

Yogodzinski G, Kelemen P (1998) Slab melting in the Aleutians: implications of an ion probe study of clinopyroxene in primitive adakite and basalt. Earth Planet Sci Lett 158:53–65

Zimmer M, Plank T, Hauri E, Yogodzinski G, Stelling P, Larsen J, Singer B, Jicha B, Mandeville C, Nye C (2010) The role of water in generating the calc-alkaline trend: new volatile data from Aleutian magmas and a new Tholeiitic Index. J Petrol. doi:10.1093/petrology/egq062